Review

Recent Progress with BCC-Structured High-Entropy Alloys

Fangfei Liu [1,2], Peter K. Liaw [3] and Yong Zhang [1,4,*]

1   Beijing Advanced Innovation Center of Materials Genome Engineering, State Key Laboratory for Advanced Metals and Materials, University of Science and Technology Beijing, Beijing 100083, China; bkdliufangfei1987@163.com
2   Dongguan Eontec Co., Ltd., Dongguan 523662, China
3   Department of Materials Science and Engineering, The University of Tennessee, Knoxville, TN 37996, USA; pliaw@utk.edu
4   Shunde Graduate School, University of Science and Technology Beijing, Foshan 528399, China
*   Correspondence: drzhangy@ustb.edu.cn

Abstract: High-entropy alloys (HEAs) prefer to form single-phase solid solutions (body-centered cubic (BCC), face-centered cubic (FCC), or hexagonal closed-packed (HCP)) due to their high mixing entropy. In this paper, we systematically review the mechanical behaviors and properties (such as oxidation and corrosion) of BCC-structured HEAs. The mechanical properties at room temperature and high temperatures of samples prepared by different processes (including vacuum arc-melting, powder sintering and additive manufacturing) are compared, and the effect of alloying on the mechanical properties is analyzed. In addition, the effects of HEA preparation and compositional regulation on corrosion resistance, and the application of high-throughput techniques in the field of HEAs, are discussed. To conclude, alloy development for BCC-structured HEAs is summarized.

Keywords: high-entropy alloys; BCC structure; refractory high-entropy alloy

1. Introduction

A new metallurgical strategy was introduced to develop advanced materials with outstanding performance—high-entropy alloys (HEAs). Today, HEAs contain five or more multiple principle metallic elements in equal or near-equal atomic percentages [1]. HEAs' four core effects [2]—high configurational entropy, sluggish diffusion, severe lattice distortion, and the cock-tail effect—are mainly responsible for their various physical and mechanical properties. HEAs present promising properties, such as high strength and fracture toughness at room temperature [3–6] and high temperatures [2,7] and have excellent wear resistance [4], and corrosion resistance [8–11], along with high-temperature oxidation [8].

HEAs are more likely to generate a simple solid solution (typically body-centered cubic (BCC), face-centered cubic (FCC), or hexagonal closed-packed (HCP) phases) despite containing many components [12–15]. Up to now, the development of HEAs has mainly gone through three stages: quinary equal-atomic single-phase solid-solution alloys; quaternary or quinary non-equal-atomic multiphase alloys; medium-entropy alloys, high-entropy fibers, high-entropy films and lightweight HEAs (LWHEAs) [16,17]. HEAs mainly include two categories: refractory elements (such as V, Cr, Ti, Mo, Nb, Ta, W, Zr, and Hf) and commodity metals (such as Cr, Co, Fe, Ni, Mn, and Cu) [18]. HEAs in the first category consist of many refractory elements, so-called refractory high-entropy alloys (RHEAs) [13], and mostly form BCC structures [19,20]. The second category of HEAs mostly forms FCC structures [21,22], a combination of FCC and BCC structures [23–25] or BCC structures alone [26,27].

However, FCC structures or "FCC-based" structure HEAs show excellent ductility high plasticity, but its yield strength is not considerable in a large number of studies reported so far [28,29]. It needs to be strengthened by a series of thermomechanical treatments before

industrial application, which requires an additional cost. In contrast to FCC HEAs, BCC HEAs exhibit relatively high intrinsic yield strengths [30,31]. Besides, RHEA systems have excellent high-temperature mechanical properties but insufficient toughness at room temperature [32,33]. Developing BCC HEAs with high strength and good ductility is a key to making them potential structural materials in technological applications.

However, it is still weak to regulate the plastic deformation behavior of BCC HEAs via the strengthening methods of FCC HEAs. BCC HEAs can only deal with liquid-solid phase transformation by some processing technology, such as melt purification, homogenization, directional solidification (DS), powder metallurgy (PM) and additive manufacturing (AM).

Nowadays, BCC HEAs have typically been fabricated via simple arc-melting and casting, which has been confirmed to be a highly efficient technique for more than five metals. For instance, the AlCrFeCoNi HEA with a single-phase BCC solid solution exhibits excellent compressive properties of yield stress (1250.96 MPa) and plastic strain (32.7%) [27]. VNbMoTa RHEAs exhibit excellent room-temperature ductility with a fracture strain > 25% and high-temperature strength (compressive yield strength of 811 MPa at 1000 °C) [34]. However, the cast product has some drawbacks including many structural defects, such as voids, porosity, chemical segregation and grain coarsening.

Powder metallurgy (PM), a forming technology that allows significant compositional accuracy can completely prevent chemical segregation, can obtain a homogeneous microstructure, can produce nanocrystalline materials and can develop metal matrix composites [35,36]. Lightweight RHEAs of CrNbVMo exhibited superior compressive specific yield strengths compared to cast RHEAs at 25 °C and 1000 °C [37]. TiNbTa$_{0.5}$Zr and TiNbTa$_{0.5}$ZrAl$_{0.2}$ RHEAs were successfully prepared without any cracks or fractures by PM, and with Al addition, the compressive peak stress increased from 508 MPa to 603 MPa at 800 °C [38]. The PM process is not only suitable for preparing RHEAs but is also suitable for preparing small and precise components.

In contrast to the conventional process, additive manufacturing (AM) is based on an incremental layer-by-layer fabrication process [39]. Because local process control can be realized in the AM process, it has extremely rapid solidification cooling rates, production with unrivaled design freedom, and shorter production cycles [40,41]. The AM process can overcome the inherent complexity and achieve the high levels of control required to produce homogeneous bulk alloys. Due to the immanent advantages of AM, it has attracted much attention in the last decade. At present, the process for preparing HEAs mainly includes direct laser deposition (DLD), selective laser melting (SLM) and selective electron beam melting (SEBM) [42–45]. The phases, crystal features, mechanical properties, functionalities and potential applications of these products have been discussed. Because the high density, low ductility at room temperature and poor resistance to oxidation are the main drawbacks of RHEAs, it is a challenge to prepare powder for the AM process.

A large number of reports on the mechanical behaviors [46,47], oxidation resistance [48,49], corrosion resistance [50,51], compositional gradient films, fibers and application of high-throughput techniques [52,53] for various BCC HEAs have been published. However, few reviews have related to the BCC HEAs. Therefore, this review aimed to summarize the various discussions around the BCC HEAs mentioned above to provide a relatively complete reference for BCC HEA researchers' future work.

The purpose of the present manuscript is to review the BCC HEAs prepared by the above three preparation processes (arc-melting, PM and AM) in recent years and their static and dynamic mechanical properties at room and elevated temperatures [46,47]. Meanwhile, special properties of BCC HEAs, such as high temperature oxidation resistance [48,49], corrosion resistance [50,51] and radiation resistance [54,55] are reviewed. Then, it briefly introduces the high-throughput techniques [52,53] for exploring the huge compositional spaces and more effectively improving the alloy development. This review aimed to summarize the various discussions around the BCC HEAs mentioned above to provide a relatively complete reference for BCC HEA researchers' future work. However, because of

the limited research reports on BCC HEAs, it is difficult to systematically discuss all aspects of it in this paper, which is also the limitation of this paper.

2. Mechanical Properties of BCC-Structured HEAs at Various Temperatures

2.1. Static Mechanical Properties

2.1.1. Processing by Vacuum Arc-Melting

To provide a relatively systematic overview of the mechanical properties of BCC-structured HEAs, their uniaxial deformation behavior is compared with traditional structural alloys, as shown in Figure 1 [56]. BCC-structured HEAs mostly consist of refractory elements, which are generally considered suitable for high-temperature applications. The RHEA systems that have been successfully prepared to date include Nb-Ta-Mo-W [13,57,58], Nb-Ti-Zr [59–66] and Nb-Ti-V [67–71].
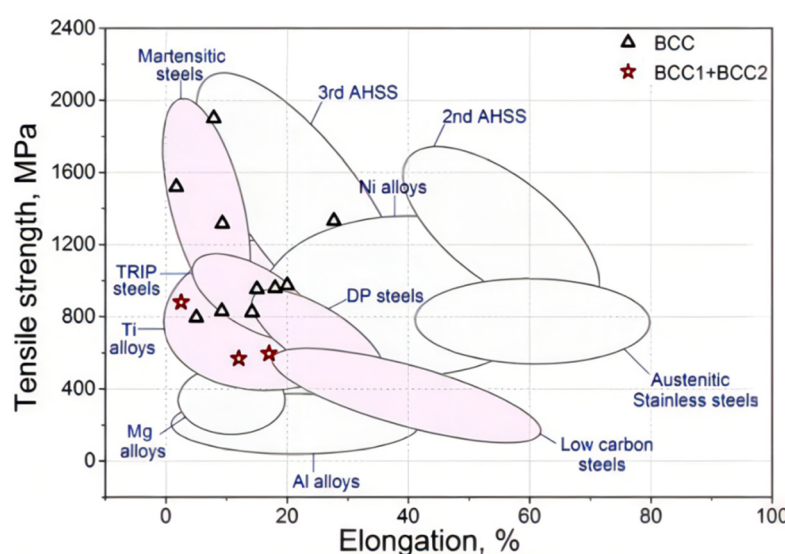

Figure 1. Room-temperature uniaxial tension test data of HEAs and CCAs with BCC, BCC1 + BCC2, 2nd and 3rd AHSS stand for the two generations of advanced high-strength steels (Reprinted with permission from ref. [56]. Copyright 2020 Elsevier).

Near-equiatomic WNbMoTa with a single-phase BCC structure was first proposed by Senkov [13], where the cast sample density and Vickers microhardness were ρ = 13.75 g/cm^3 and Hv = 4455 MPa, respectively. The alloy possessed a compressive yielded strength of 1058 MPa [59] failed by splitting at ε_p = 2.1% at an ambient temperature and decreased in yielded strength to 561 MPa and 552 MPa when the samples deformed at 600 °C and 800 °C, respectively (Figure 2) [57]. Then, single-crystalline HEA pillars on samples' surfaces were prepared with high compressive strength (~4–4.5 GPa) and lower size dependence by Zou et al. (Figure 3) [72], which could have been achieved by higher lattice friction caused by localized distortion at atomic length scales. Compared with the TaNbMoW HEA [63], the specific yield strength (SYS = σ_y/ρ) of TaNbHfZrTi HEA [59] is superior to the SYS of the TaNbMoW alloy in the temperature range of 296~1073 K (929~535 MPa). When the test temperature exceeds 1073 k, the yield strength of the TaNbHfZrTi HEA with a much lower melting temperature decreases rapidly. Yao et al. [68] calculated and designed NbTaTiV, NbTaVW and NbTaTiVW with a single phase, and the results showed that NbTaTiV exhibits exceptional compressive ductility (~50%) at room temperature and a yield strength of 965 MPa, while NbTaTiVW and NbTaVW show yield strengths of 1420 MPa and 1530 MPa with fracture strains of 20% and 12%, respectively (Figure 4). Work hardening can be observed in these HEAs.
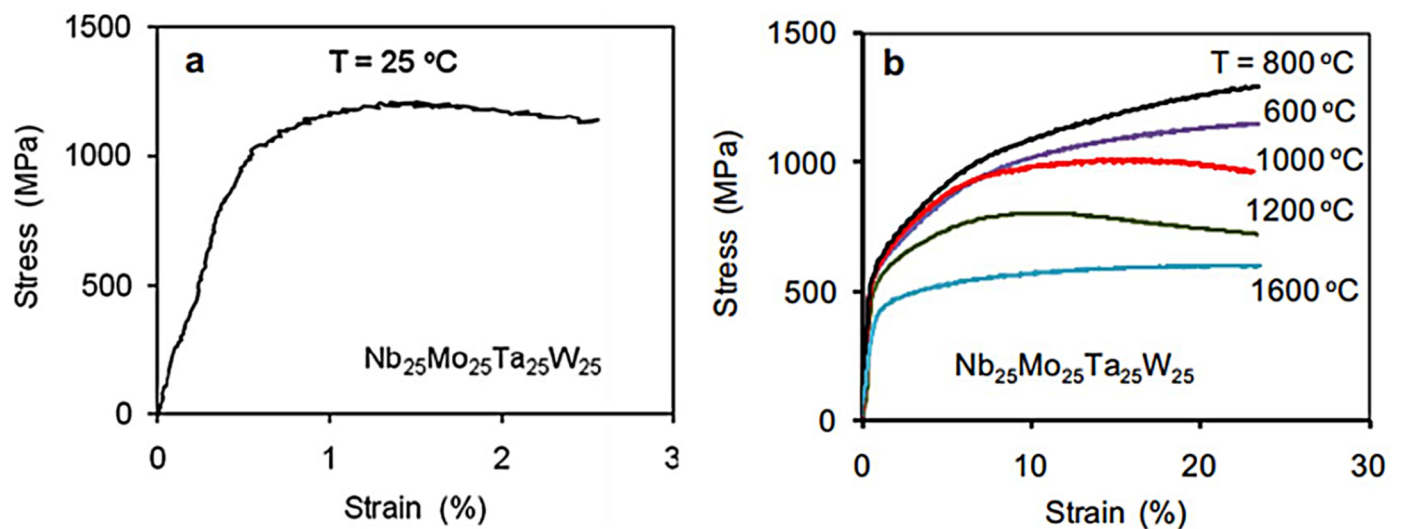
Figure 2. Compressive engineering stress-strain curves for the $Nb_{25}Mo_{25}Ta_{25}W_{25}$ alloy obtained at (**a**) room temperature and (**b**) elevated temperatures (Reprinted with permission from ref. [57]. Copyright 2011 Elsevier).
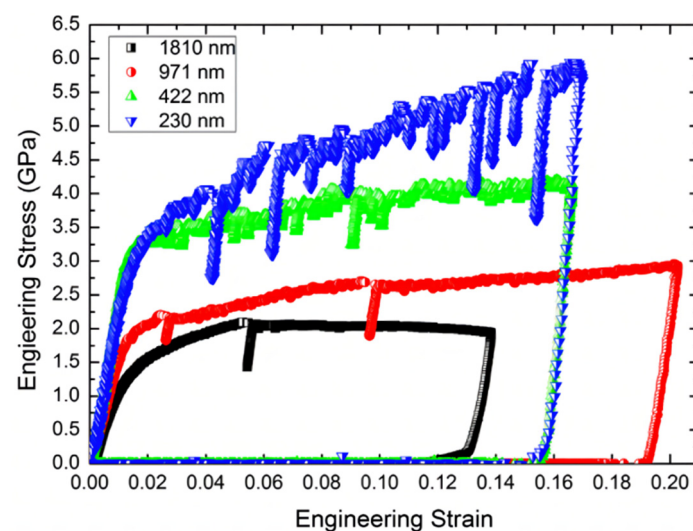

Figure 3. Representative engineering stress strain curves for [1]-oriented single crystalline HEA pillars with diameters ranging from ~2 μm to ~200 nm (Reprinted with permission from ref. [72]. Copyright 2014 Elsevier).

The alloying method is also widely used to enhance the mechanical properties of HEAs. The refractory elements (Nb, V, and Zr), Ti and Al with low density are the most commonly used alloying elements to improve the specific yield strength. Ti elements and their alloys possess good ductility and excellent high-temperature properties [73]. For example, the solid-solution hardening effect of Ti addition is beneficial to the compressive strength and ductility of NbMoTaW and VNbMoTaW HEAs at room temperature. The yield strengths of TiNbMoTaW and TiVNbMoTaW are ~586 and ~659 MPa at 1200 °C (Figure 5), respectively [73], so they are expected to be used as materials for high-temperature applications. At room temperature, the compressive yield strengths of $Ti_{20}Zr_{20}Hf_{20}Nb_{20}V_{20}$ and $Ti_{20}Zr_{20}Hf_{20}Nb_{20}Cr_{20}$ as-cast alloys [65] are 1170 and 1375 MPa, respectively. Compared with the addition of V, the addition of Cr will form Laves phase precipitation in the BCC matrix and achieve strengthening. Besides this, the structural and mechanical properties of two HEAs remained stable after a short period (10 min) of heat treatment at a high temperature, as shown in Figure 6. Substituting Hf and Cr in the $CrMo_{0.5}NbTa_{0.5}TiZr$

and HfNbTaTiZr HEAs can reduce these alloys' density and improve the RT strength and ductility [61].

In addition to the RHEAs mentioned above, there are few other HEA systems. For example, TiAlFeCoNi HEA [73] with the L2$_1$-BCC crystal structure was prepared by arc-melting and further processed by the high-pressure torsion (HPT) method. Moreover, the alloy exhibited ultrahigh hardness (880 Hv), low elastic modulus (123–129 GPa) and superior activity for cell proliferation.

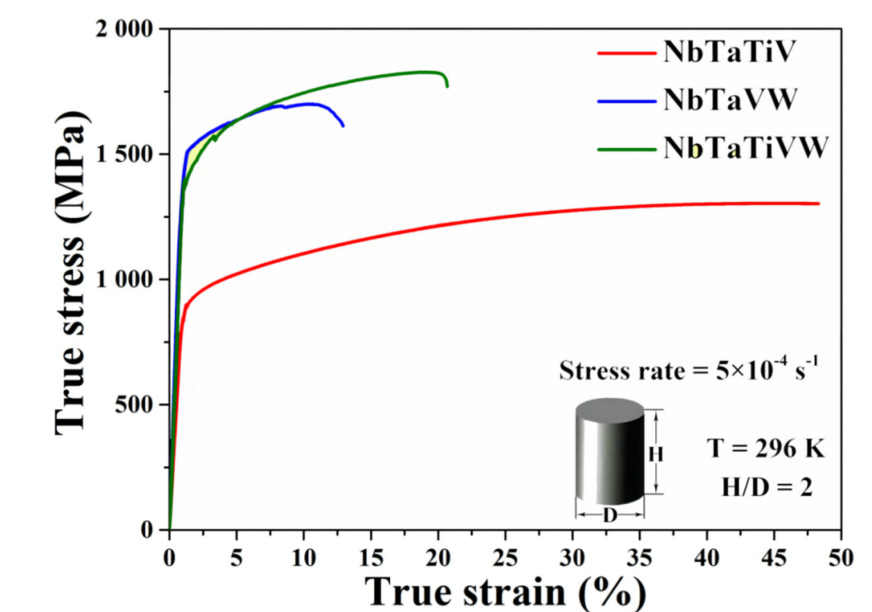**Figure 4.** Compressive engineering stress-strain curves for HEAs NbTaTiV, NbTaVW, and NbTaTiVW at room temperature (Reprinted with permission from ref. [68]. Copyright 2016 Elsevier).
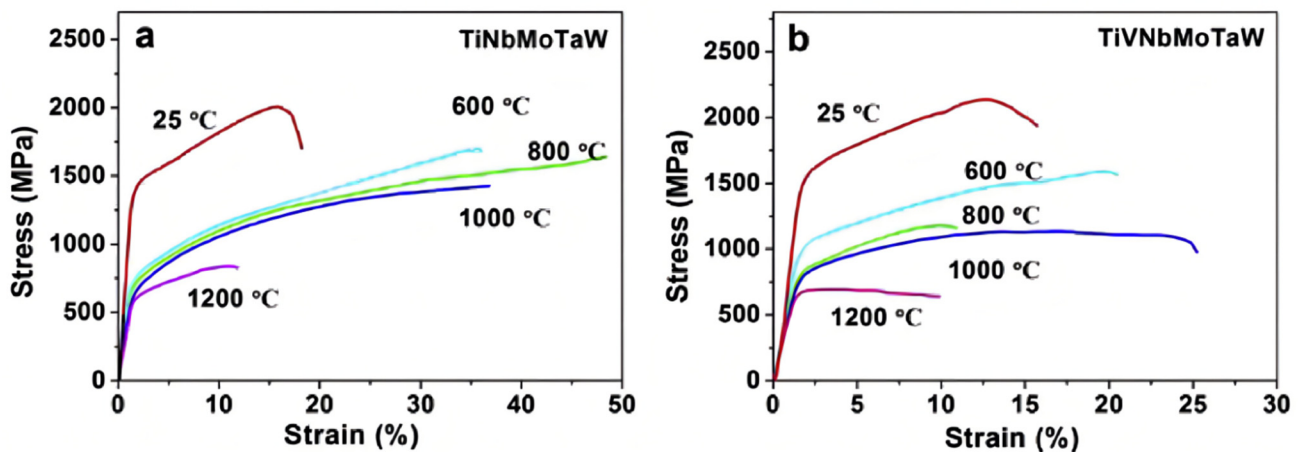

Figure 5. The compressive stress-strain curves of the TiNbMoTaW (**a**) and TiVNbTaMoW (**b**) HEAs at room temperature and elevated temperatures (Reprinted with permission from ref. [73]. Copyright 2017 Elsevier).
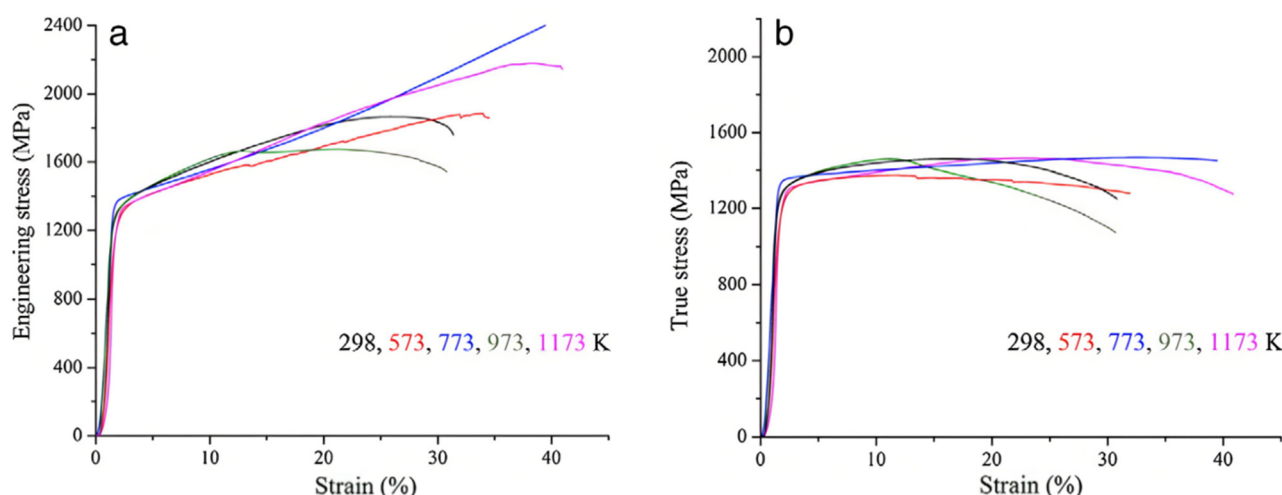
Figure 6. Engineering stress and true stress vs. strain compression curves for the $Ti_{20}Zr_{20}Hf_{20}Nb_{20}V_{20}$ (**a**,**b**) and $Ti_{20}Zr_{20}Hf_{20}Nb_{20}Cr_{20}$ alloys in the as-cast (Reprinted with permission from ref. [65]. Copyright 2014 Elsevier).

2.1.2. Processing by Powder Metallurgy

These samples in the reports mentioned above were prepared by using the vacuum arc-melting technique. Mechanical alloying (MA) with spark plasma sintering (SPS) [74–76], as a typical technology of PM, can readily fabricate bulk high-density HEAs with ultrafine grains, excellent microstructural homogeneity, improved strength and hardness. $Nb_{25}Mo_{25}Ta_{25}W_{25}$ and $Ti_8Nb_{23}Mo_{23}Ta_{23}W_{23}$ HEAs [77] were successfully prepared by MA with SPS technology. The compressive yield stress and fracture strain of $Nb_{25}Mo_{25}Ta_{25}W_{25}$ HEAs with average grain sizes ~0.88 μm are 2460 MPa and 16.8%, which are remarkably superior to those prepared by casting [57]. However, coarse grain size is conducive to the improvement of high-temperature strength, which is mainly attributed to the fact that the grain boundary is the weak area and plays as the flow unit at high temperatures [78]. Besides this, the addition of Ti can facilitate the grain refinement and Ti particles distributed at grain boundaries can improve the toughness of the $Ti_8Nb_{23}Mo_{23}Ta_{23}W_{23}$ HEA (2377 MPa, 26.3%). The WNbMoTaV HEA [79], when sintered, shows an ultra-high compressive yield strength of 2612 MPa with a failure strain of 8.8% at room temperature, respectively. Meanwhile, Long et al. [80] reported that Laves phase precipitated in the BCC matrix of NbMoTaWVCr HEA and enhanced its mechanical properties by introducing Cr to the WNbMoTaV HEA. Laves phase formed in the BCC matrix due to the smaller atomic radius of Cr compared with the other alloy elements in those RHEAs [60,64,81]. The compressive yield strength (3416 MPa) of the bulk NbMoTaWVCr HEA is dramatically higher than those of the previously reported refractory HEAs fabricated by casting and powder metallurgy methods, as shown in Figure 7. The outstanding mechanical properties of the WNbMoTaV HEA were attributed to fine-grain strengthening, intrinsic and interstitial solid solution strengthening and Orowan strengthening. The enhancement in yield strength of the NbMoTaWVCr HEA may result from the combined effects of finer grain size, a homogeneous microstructure and enhancement of atomic size misfit caused by the addition of Cr and interstitial solid solution strengthening from O (O was inevitably introduced into the mechanically alloyed powders).
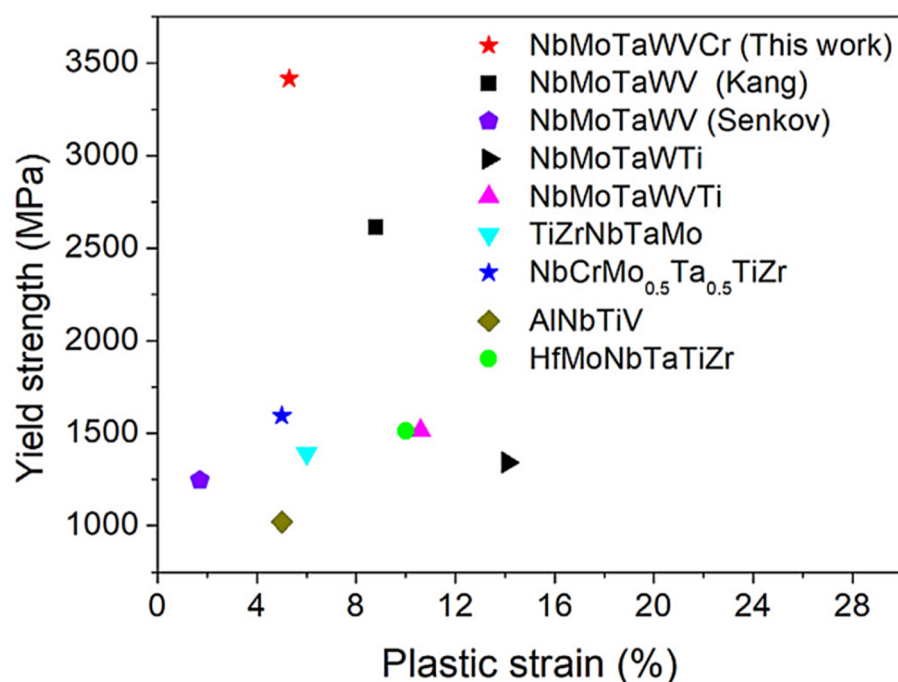
Figure 7. Plots of compressive yield strength and plastic strain of typical refractory HEAs at room temperature (Reprinted with permission from ref. [80]. Copyright 2019 Elsevier).

In addition to the WNbMoTa HEA, BCC-structured HEA systems prepared by MA with SPS technology also include AlFeTiCrZnCu [82–84], CrTiVTaW [19,85], TiNbTaZr [38] and FeCrMnV [17,86,87]. The AlFeTiCrZnCu HEA [84] prepared by MA with SPS technology can achieve a 99% density and homogeneous nanostructure (~10 nm) and its hardness can reach 2 GPa.

The effect of Ti on the phase structure and mechanical properties of $Ti_xWTaVCr$ HEA [85] was studied: a single BCC solid solution could be formed when the Ti content was up to 7%. Compared with pure W and several other HEAs, $Ti_7WTaVCr$ has higher room-temperature and high-temperature compressive yield strengths, owing to solid solution strengthening and the effects of Cr and V.

Cao et al. [38] successfully prepared TiNbTa0.5Zr and $TiNbTa_{0.5}ZrAl_{0.2}$ HEAs with a single BCC phase using powder metallurgy technology. The compressive yield strength and strain for $TiNbTa_{0.5}Zr$ and $TiNbTa_{0.5}ZrAl_{0.2}$ alloys at room temperature were 1310 MPa, 30% and 1500 MPa, 30%, respectively. Figure 8 compares the compressive properties of these HEAs with those of available refractory HEAs. $TiNbTa_{0.5}Zr$ and $TiNbTa_{0.5}ZrAl_{0.2}$ present a good combination of strength and plasticity, while most refractory HEAs still follow the strength-ductility trade-off. Besides this, $TiNbTa_{0.5}Zr$ and $TiNbTa_{0.5}ZrAl_{0.2}$ HEAs show a compressed maximum engineering strain of 50% without any cracking or fractures at 800 °C. Moreover, the NbTaTiV HEA exhibits a compressive yield strength of 1.37 GPa and a high fracture strain of 23% at room temperature. When deformation occurs at 1000 C, it still exhibits a high yield strength of 437 MPa with a compression strain of over 40%. Its outstanding mechanical properties are mainly attributed to the homogeneous and fine microstructures and solid solution strengthening effect.
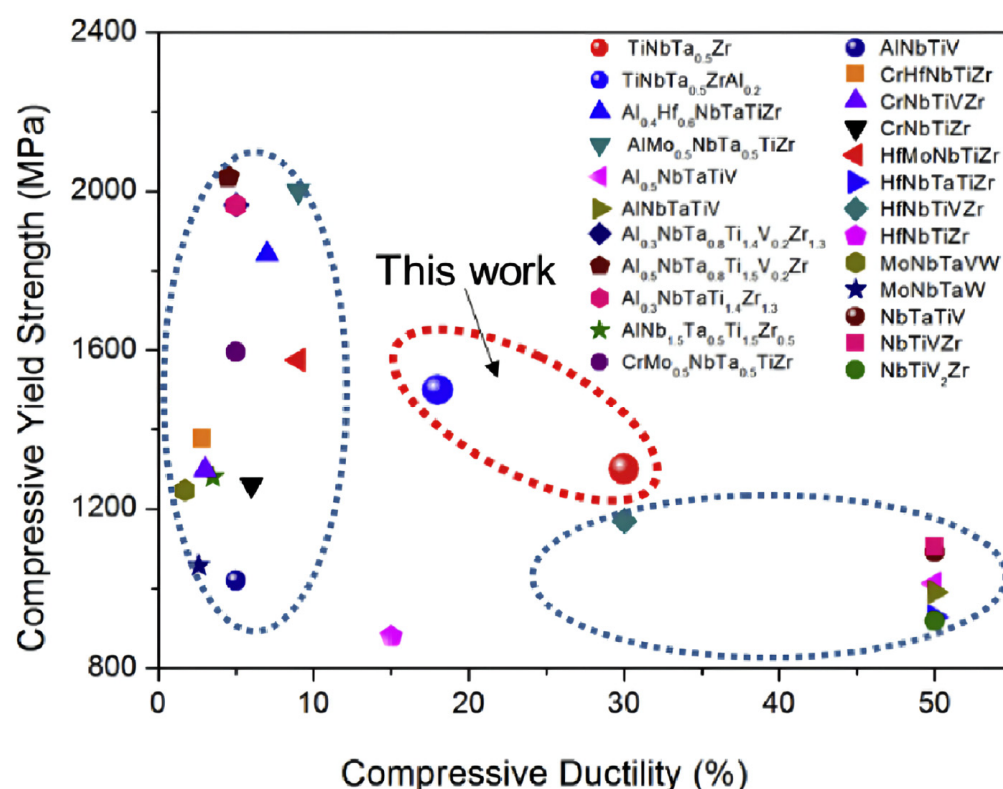
Figure 8. Compressive properties of the refractory high-entropy alloys obtained at room temperature; compressive yield strength vs. compressive ductility (Reprinted with permission from ref. [38]. Copyright 2018 Elsevier).

The volume fraction of the BCC2 phase gradually increased with the increase in the Al concentration in AlxCrFeMoV HEAs [88]. The improvement of compressive yield strength from 2730 to 3552 MPa can be attributed to the solid solution strengthening of Al caused by the appearance of the BCC2 phase. The addition of Al dually influenced the properties of the CrFeMoV alloy by improving its strength and reducing the density of the system. The yield strength and hardness as a function of density were compared with data for previously reported HEAs (Figure 9). AlxCrFeMoV HEAs with outstanding mechanical properties, a low cost and low density, which are better than those of any previously reported HEAs, suggested a promising future for the HEAs in many structural applications.

In another case, new phases appeared in the BCC matrix, such as the B2 phase, HCP phase and FCC phase, after SPS processing. As reported [17], AlCuFeMnTiV HEA prepared by sintering powder containing only the BCC phase has the B2 phase, HCP phase and Cu-rich FCC phase precipitated at the grain boundary in addition to the BCC matrix. It exhibits the best comprehensive mechanical properties, with a density of 6.28 g/cm^3, compressive yield strength of 2060 MPa and plastic strain of 15.83%, which are superior to most LWHEAs and traditional lightweight alloys. The high strength and good plasticity of AlCuFeMnTiV HEAs are attributed to the strengthening effect of nano twins precipitated in the FCC phase on grain boundaries.

The above discussion demonstrates that powder metallurgy is a promising way of preparing ductile RHEAs with outstanding comprehensive mechanical properties.
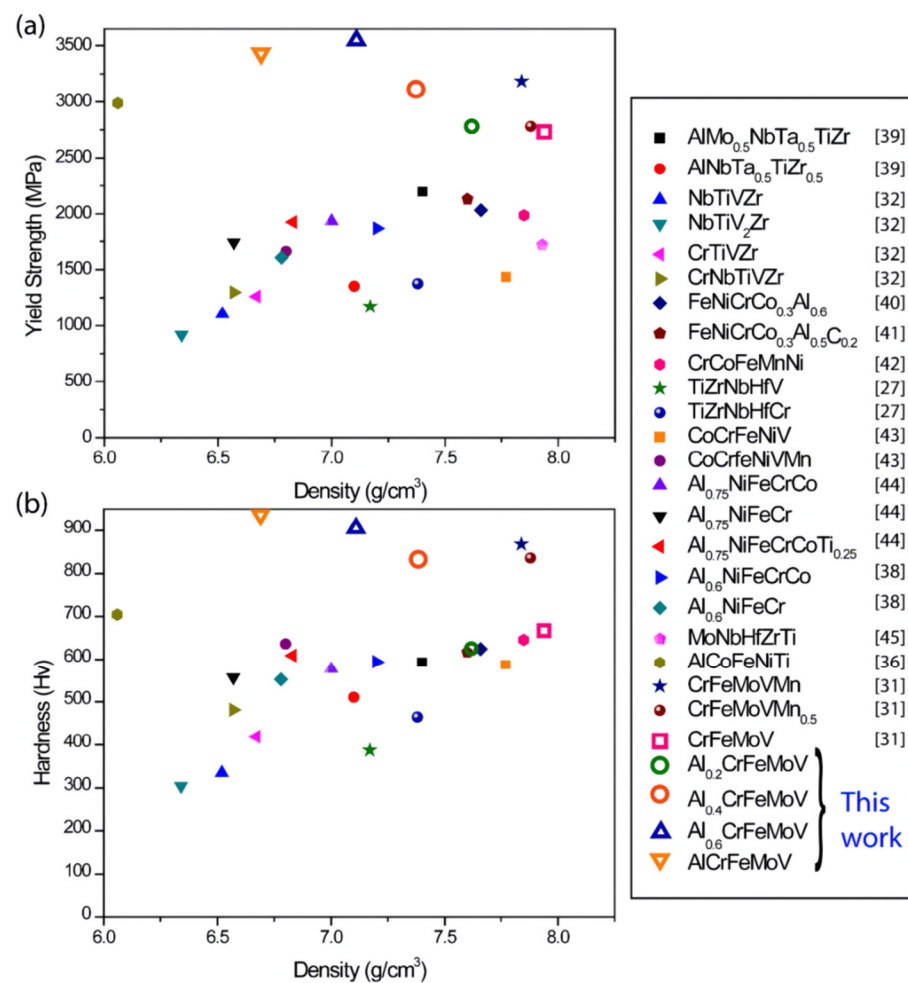
Figure 9. (**a**) Compressive yield strength and (**b**) hardness as a function of density for the current alloys and previously reported high-entropy alloys (HEAs) (Reprinted with permission from ref. [88]. Copyright 2018 Elsevier).

2.1.3. Processing by Additive Manufacturing

Recently, several attempts have been made to prepare BCC-structured HEAs (mainly RHEAs) by laser deposition techniques, and there have been many studies on the preparation of those HEAs by arc-melting and PM. The attempts to prepare BCC structure HEAs using AM technology have mainly been based on DLD technology, and few reports have been published on SLM or SEBM.

The process of DLD may also be known as laser metal deposition (LMD), direct metal deposition (DMD), laser engineered net shaping (LENS) and laser cladding. The MoNbTaW RHEA [89] with single-wall structures was the first BCC-structured alloy system to be prepared by the DLD method. The case indicated that it is feasible to fabricate a RHEA through in situ alloying of a Mo-Nb-Ta-W elemental mixture even if cracks appear during processing. The bulk of the crack-free TiZrNbTa RHEAs [90] was successfully produced by in-situ alloying of elemental powders using the DLD method. It is one of the few alloy systems with suitable room temperature plasticity among the RHEAs. A well-defined compositional gradient with good hardness (440 HV0.1) was obtained by optimizing the DLD method, as shown in Figure 10.
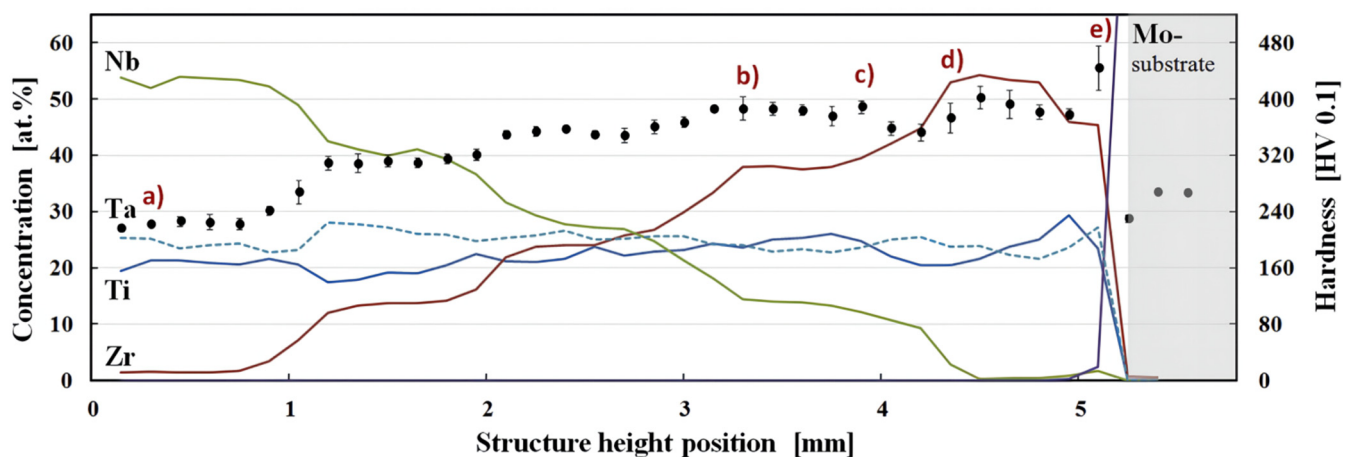
Figure 10. Compositionally graded material produced from five modified powder blends with linearly changing compositions from $Ti_{23}Zr_{43}Nb_0Ta_{34}$ to $Ti_{23}Zr_0Nb_{42}Ta_{35}$ (Reprinted with permission from ref. [90]. Copyright 2019 Elsevier).

SLM, as a typical AM technology, can three-dimensionally (3D) fabricate components with intricated shapes and refined resolutions [91–93]. The fabrication of BCC-structured HEAs through the SLM process has rarely been considered. A MoNbTaW refractory HEA was prepared via the SLM process using blended elemental powders [45,94]. There was a deviation between the chemical composition of the prepared sample and that of a premixed powder. This was likely due to surface evaporation of the lower melting-point elements which floated to the upper surface of the melt pool during the SLM process. Composition partitioning was in direct contrast with that reported by Dobbelstein et al. [83] for MoNbTaW HEAs fabricated via DLD.

The operating principle was similar to that of SLM, but SEBM used an electron beam instead of a laser beam as the heat source, which meant it has attracted extensive attention in recent years. SEBM has the unique characteristics of a high energy density of the incident electron beam, high scan speed, and moderate operation cost and so on. In addition, the high temperature preheating (up to 1100 °C) of the powder bed by the electron beam prior to scanning and melting is another distinct working condition of SEBM. This working condition results in low residual stress of the built products, making the SEBM process suitable to fabricate complex shaped products and reducing the thermal cracking and distortion of the printed-HEAs [95–97].

Hiroshi et al. [96] investigated the microstructures and mechanical properties of equiatomic AlCoCrFeNi HEA samples fabricated by SEBM comparing them with those of samples prepared by arc-melting. The proportion of the FCC phase (precipitated at the grain boundaries of the B2/BCC grains) for the bottom was much higher than that for the top. Therefore, the hardness of the SEBM samples gradually decreased with an increased proportion of the FCC phase, and they exhibited much higher plastic deformability than the cast specimen, without a significant loss of strength (Figure 11). Wang et al. precipitated CoCrFeNiMn HEA via EBM, the tensile properties of which (average YS ~205 MPa, elongation ~63%) were almost the same as those of the as-cast form obtained by He et al. [98]. The $Al_{0.5}CrMoNbTa_{0.5}$ HEAs [43] from elemental powder blends were prepared using the SEBM technique. By optimizing the process parameters, the porosity was reduced to replace the post-treatment in the traditional processing technology. However, the simultaneous handling of several elemental or pre-alloyed powders brings new challenges to the deposition process.
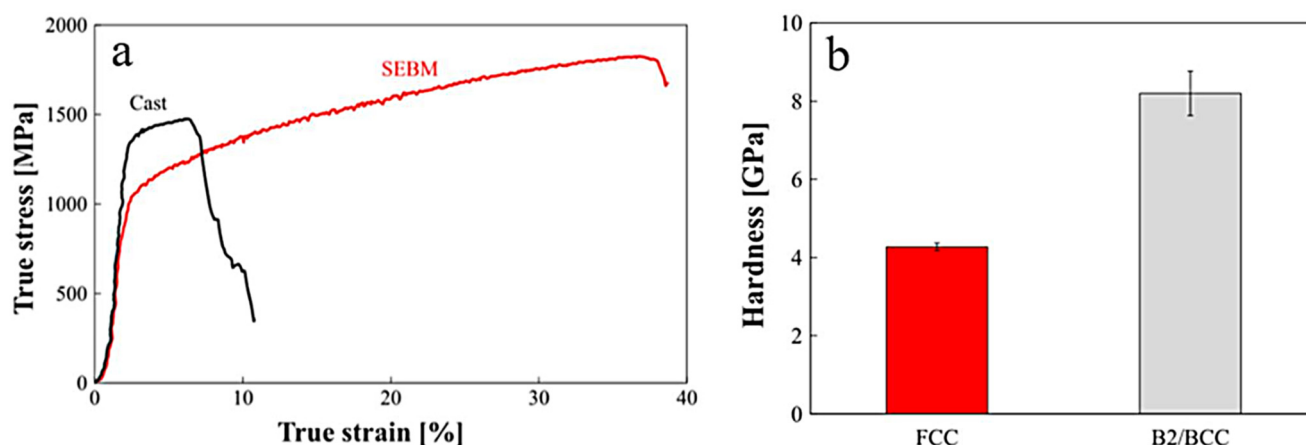
Figure 11. (**a**) Compressive stress-strain curves of the cast and SEBM specimens and (**b**) nanohardness of the FCC and B2/BCC phases measured at the bottom of the SEBM specimens (Reprinted with permission from ref. [96]. Copyright 2016 Elsevier).

2.1.4. Self-Sharpening

The previous three parts of the article mainly summarized the BCC-structured HEAs prepared by three forming methods, largely focusing on their tensile or compressive properties under quasi-static conditions, while it is the dynamic tensile or compressive properties that affect its self-sharpening.

"Self-sharpening" is the ability of the material to maintain its acute head shape during penetration, which is a necessary property of material during armor-piercing [99]. HEAs possess a good combination of strength and ductility, which is the premise of excellent self-sharpening. Besides this, high susceptibility to adiabatic shear banding (ASB) is the fundamental cause of self-sharpening behavior that benefits penetration performance [100,101]. ASB is the dominant deformation mechanism for materials consisting of metals or alloys under high-strain-rate loading, which exhibits a narrow band where large shear deformation occurs in a very short time [102–105].

At present, the research on self-sharpening mainly focuses on W-based alloys [106,107]. W-based alloys are promising candidates for kinetic energy penetrators because of their high density, strength, and ductility [108,109]. However, the low susceptibility of W-based alloys to ASB reduces their penetration depth. Thus, it is necessary to develop a new matrix material to replace W-based alloys. The sluggish diffusion and lattice distortion effect of HEAs can achieve a balance between strength and toughness and improve the penetration ability [110]. This means that HEAs can be used as potential materials with excellent self-sharpening properties. However, only limited success has been achieved in the development of new tungsten HEAs. A new chemical-disordered multi-phase tungsten HEA (WFeNiMo) was developed by Liu et al. [99]. Compared with conventional W-based alloys, WFeNiMo consists of a BCC dendrite phase and a rhombohedral μ phase embedded in the continuous FCC matrix, which means it exhibits outstanding self-sharpening capability, as shown in Figure 12. This is due to the precipitation of the ultra-strong μ phase of WFeNiMo, which can mediate the shear banding by triggering dynamic recrystallization softening. Subsequently, Chen et al. [106] conducted experiments with WFeNiMo HEA and W-based alloy projectiles penetrating medium-carbon steel by using a ballistic gun and a two-stage light-gas gun. As the impact velocity increased (1330 m/s~1531 m/s.), the penetration mode of the WFeNiMo HEA projectile changed from self-sharpening to mushrooming.
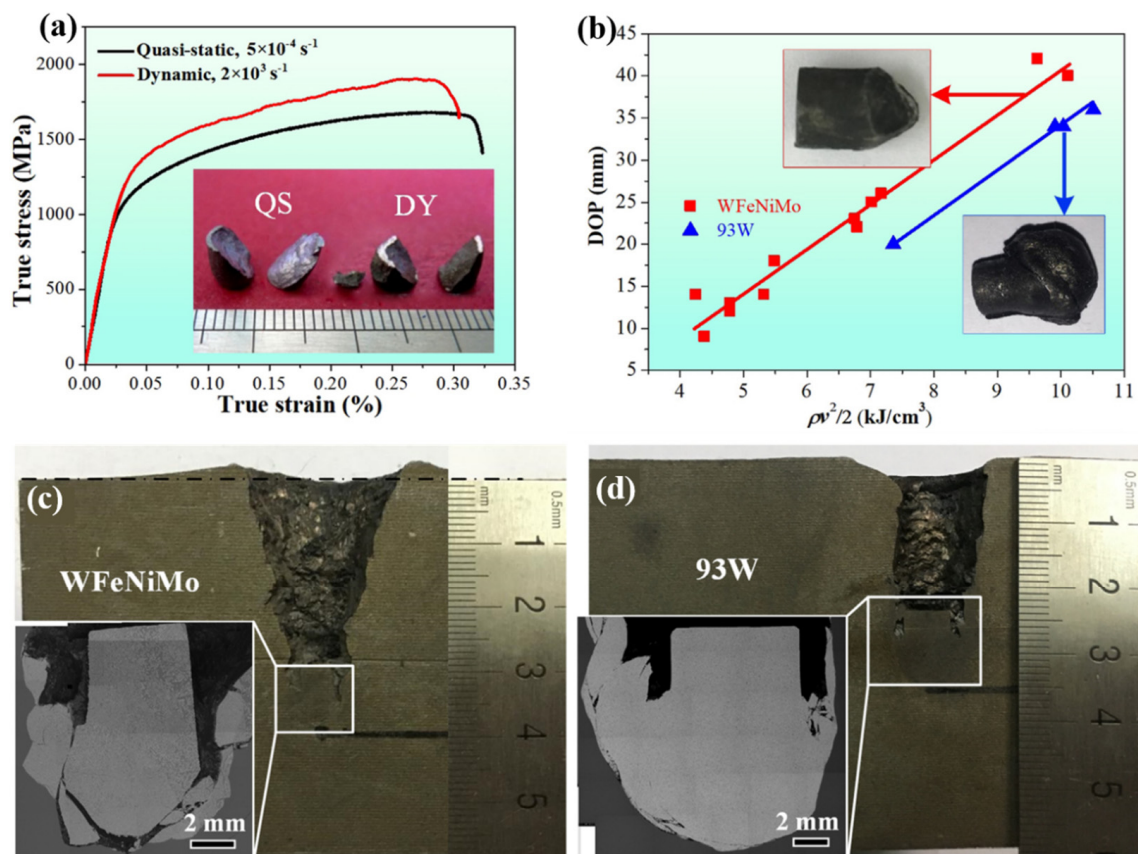
Figure 12. (**a**) Compressive stress-strain curves of alloys under quasi-static and dynamic conditions, with macroscopic fracture samples in the inset; (**b**) Depth of penetration of WFeNiMo rod and 93 W rod versus kinetic energy per volume calculated by $\rho v2/2$, with photographs of the retrieved remnants, respectively; Longitudinal sections of medium carbon steel targets impacted by (**c**) a WFeNiMo penetrator and (**d**) a 93 W penetrator, with SEM micrographs of the remnant in the corresponding insets, respectively (Reprinted with permission from ref. [99]. Copyright 2020 Elsevier).

In general, BCC structure HEAs can be successfully fabricated by arc-melting and PM (MA with SPS technology), but the preparation of pre-alloyed powder is still one of the difficult problems for the attempt of AM technology. BCC structure HEAs have ultrahigh strength, high hardness and room temperature plasticity, which has been gradually improved in recent studies. It has great potential in aerospace, military (high performance penetrator materials) and biomedical fields in future applications.

3. Special Properties of BCC-Structured High-Entropy Alloys

3.1. Oxidation

As the main part of BCC-structured HEAs, RHEAs are promising candidates for new-generation high-temperature materials. Yet, RHEAs have two fatal disadvantages: room temperature brittleness and unsatisfactory high-temperature oxidation resistance. Early research [111–113] focused on improving the high-temperature oxidation resistance of RHEAs by adding elements, such as Al, Cr and Si. However, this tends to promote the formation of intermetallic compounds, such as Al_2O_3, Cr_2O_3 and SiO_2, which worsen the poor room-temperature ductility. In this context, it presents a challenge to enhance the oxidation resistance and achieve optimal room-temperature ductility at the same time for RHEAs.

Müller et al. [49] systematically investigated the oxidation behavior of four refractory HEAs within the system of the Ta-Nb-Mo-Cr-Ti-Al RHEA (including TaMoCrTiAl, NbMoCrTiAl, NbMoCrAl and TaMoCrAl) at 900 and 1100 °C in the air. Because of the

formation of protective Al_2O_3, Cr_2O_3 and $CrTaO_4$ oxide layers, the TaMoCrTiAl RHEA shows superior oxidation resistance at 1000 °C in the air (Figure 13). Moreover, the addition of Ti can effectively improve the oxidation resistance of the RHEA [48,85,114] which is attributed to promoting the formation of protective rutile type oxides and reducing the formation of less favorable oxides. However, the oxidation resistance of the RHEAs is significantly reduced with V addition [48,114]. It is mainly due to the addition of V that the oxide scales become porous for the other RHEAs, aggravating the volatility of V_2O_5 and leading to disastrous internal oxidation.
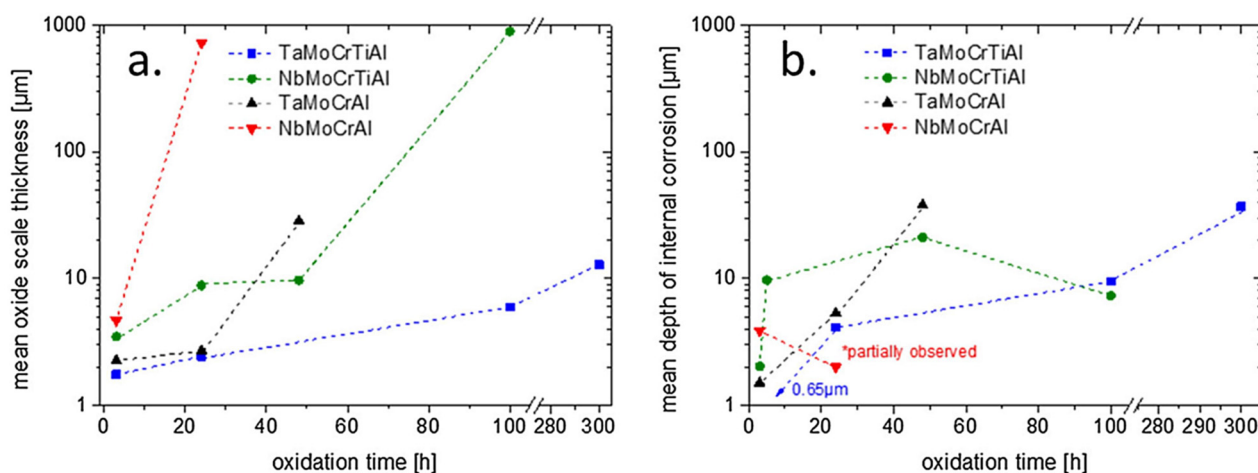

Figure 13. Mean oxide scale thickness (**a**) and mean depth of internal corrosion (**b**) for TaMoCrTiAl, NbMoCrTiAl, TaMoCrAl, and NbMoCrAl during isothermal exposure to air at 1000 °C (Reprinted with permission from ref. [49]. Copyright 2019 Elsevier).

Those results add a crucial perspective to the further development of RHEAs as novel high-temperature materials, with balanced room-temperature ductility and high-temperature oxidation resistance.

3.2. Corrosion

To the best of our knowledge, two papers [50,115] have reviewed the corrosion of HEAs. HEAs exhibit much better corrosion resistance than traditional corrosion-resistant metal materials, e.g., stainless steel, copper-nickel alloys, and high-nickel alloys, attributed to the high-entropy and cocktail effects, in particular. Therefore, the corrosion resistance of HEAs has attracted extensive attention in the field of corrosion research.

Qiu et al. [115] reviewed the influence of metal elements (including aluminum, titanium, chromium, molybdenum and nickel) and processing methods (anodizing and aging) on the corrosion resistance of HEAs. $AlMo_{0.5}NbTa_{0.5}TiZr$ HEA [51] exhibited extensive segregation of alloying elements and significant gradients in local chemistry, which lend it excellent corrosion characteristics, as shown in Figure 14. Fu et al. [50] further reviewed the corrosion behaviors and mechanisms of HEAs in various aqueous solutions, discussed the effects of heat treatment, anodizing treatment and preparation methods on the corrosion behaviors of HEAs, and established correlations between the composition, microstructure and corrosion resistance of HEAs.
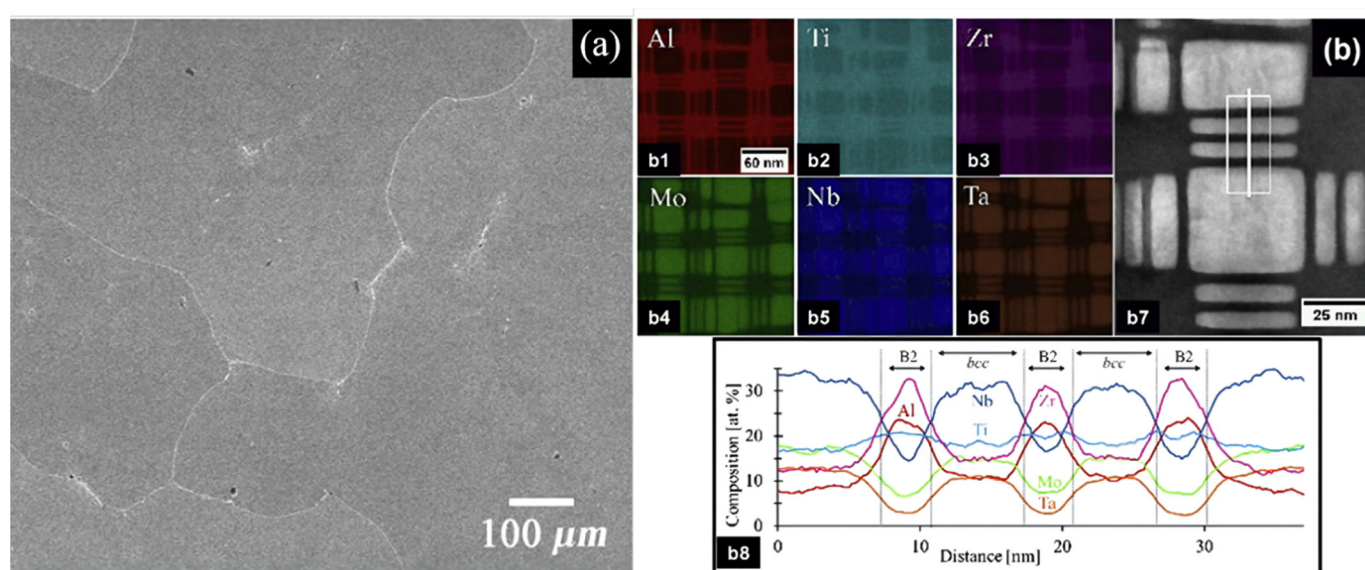
Figure 14. (**a**) (Reprinted with permission from ref. [116]. Copyright 2016 Elsevier) SEM micrograph of an as-cast Al$_{0.3}$CoCrFeNi showing a single-phase microstructure and (**b**) (Reprinted with permission from ref. [51]. Copyright 2016 Elsevier) (**b1**–**b6**) XEDS elemental maps of Al, Ti, Zr, Mo, Nb and Ta, respectively, recorded in STEM using the Super-X™ detector, while (**b7**) is a STEM-HAADF image with a white line identifying the location of the EDXS line scan shown in (**b8**).

The electrochemical behaviors of the AlCoCrFeNi HEA [97] obtained with SEBM were investigated, which were influenced by the phase morphologies. The pitting potential of SEBM specimens (0.112 V vs. Ag/AgCl) was lower than that of a cast specimen (0.178 V vs. Ag/AgCl). Equiatomic TiZrNbTaMo RHEA [117] as cast samples underwent a study of their corrosion resistance, to investigate whether they met the requirements of orthopedic implants. Compared with Ti6Al4V, 316LSS and CoCrMo alloys, TiZrNbTaMo HEA exhibited excellent corrosion resistance (Figure 15) in a phosphate buffer solution (PBS) and potentially excellent biocompatibility, attributed to the surface passivation and high stability, regardless of the pitting. It has preliminary advantages in mechanical properties and corrosion resistance and can offer an opportunity to explore new orthopedic-implant alloys.

3.3. Irradiation

Under the condition of irradiation, structural materials are faced with the interaction between irradiated particles (ions, neutrons, electrons, etc.) and lattice atoms of the material itself, which leads to the formation of irradiation defects and the evolution of microstructure and then affects the service performance of the material. Among them, the most difficult problem is volume swelling [54,55,118]. HEAs have the advantages of being an irradiation resistant material because of their high-temperature phase structure stability, high-temperature softening resistance, high-temperature oxidation performance and corrosion resistance comparable to that of austenitic stainless steel.

As a general rule, BCC alloys exhibit superior resistance to void swelling, primary defect production and defect evolution behaviors than FCC alloys [119–121]. Compared with FCC alloys, the peak in BCC alloys swelling is often found at comparatively low homologous temperatures when they do undergo void swelling and their temperature dependence of swelling can be quite different [122,123]. Because of higher atomic diffusivities, BCC alloys tend to have a higher speed in the diffusion dependent process [124]. Therefore, BCC structure HEAs have attracted extensive attention because of their unique high temperature stability and radiation resistance.
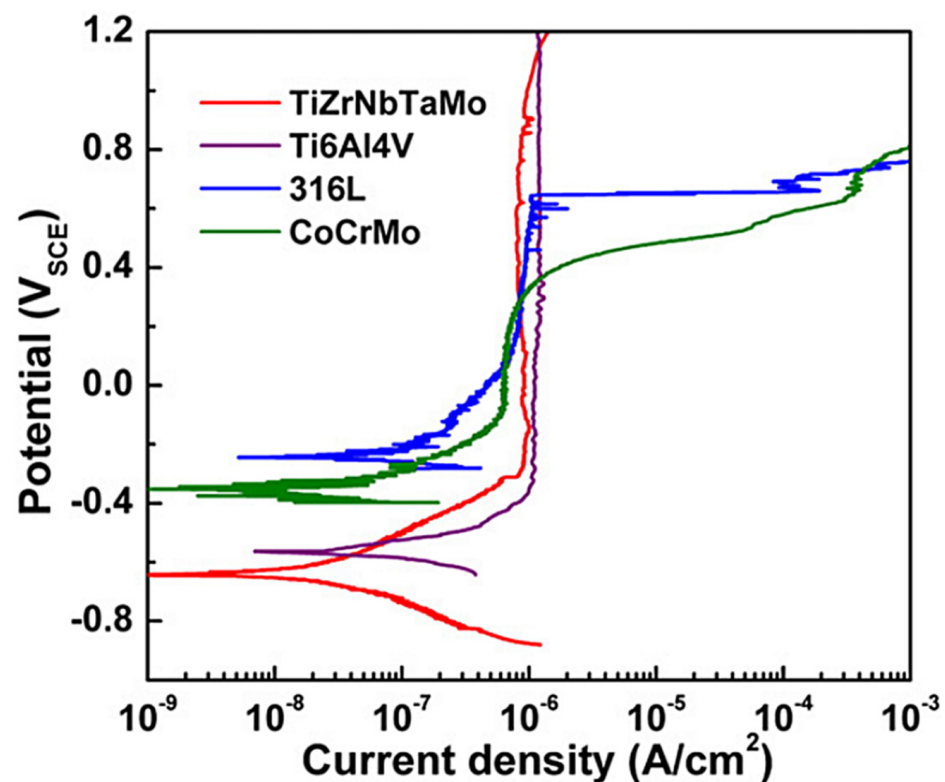
Figure 15. Potentiodynamic polarization curves of arc-melted TiZrNbTaMo HEA, as well as Ti6Al4V, 316L SS and $Co_{28}Cr_6Mo$ alloys in PBS at 37 °C for comparison (Reprinted with permission from ref. [117]. Copyright 2016 Elsevier).

A BCC structure W-based RHEA film with outstanding radiation resistance has been prepared by O. El-Atwani [125]. In their work, the films with uniform composition have element segregation at the grain boundary after irradiation, and the precipitation of Cr rich and V rich phases occurs in the grains. The hardness of the deposited film is about 14 GPa, and the hardness polarization does not change after heat treatment and irradiation, indicating that the alloy has excellent radiation softening resistance and can maintain the stability of the microstructure.

Two novel BCC structured $Mo_{0.5}NbTiVCr_{0.25}$ and $Mo_{0.5}NbTiV_{0.5}Zr_{0.25}$ HEAs were fabricated by vacuum arc-melting [126]. Zhang et al. investigated the crystal structure, hardness, and microstructure evolution by performing on the two HEAs to simulate neutron irradiation with Helium-ion irradiation. The two HEAs showed slight irradiation hardening compared with most of the conventional alloys (as shown in Figure 16). The helium bubbles and dislocation loops with small sizes were observed in the two HEAs after irradiation. This is the first time to report the formation of a dislocation loop in BCC structure HEAs after irradiation. $Mo_{0.5}NbTiVCr_{0.25}$ and $Mo_{0.5}NbTiV_{0.5}Zr_{0.25}$ HEAs show outstanding irradiation resistance, which may be promising accident-tolerant fuel cladding materials.
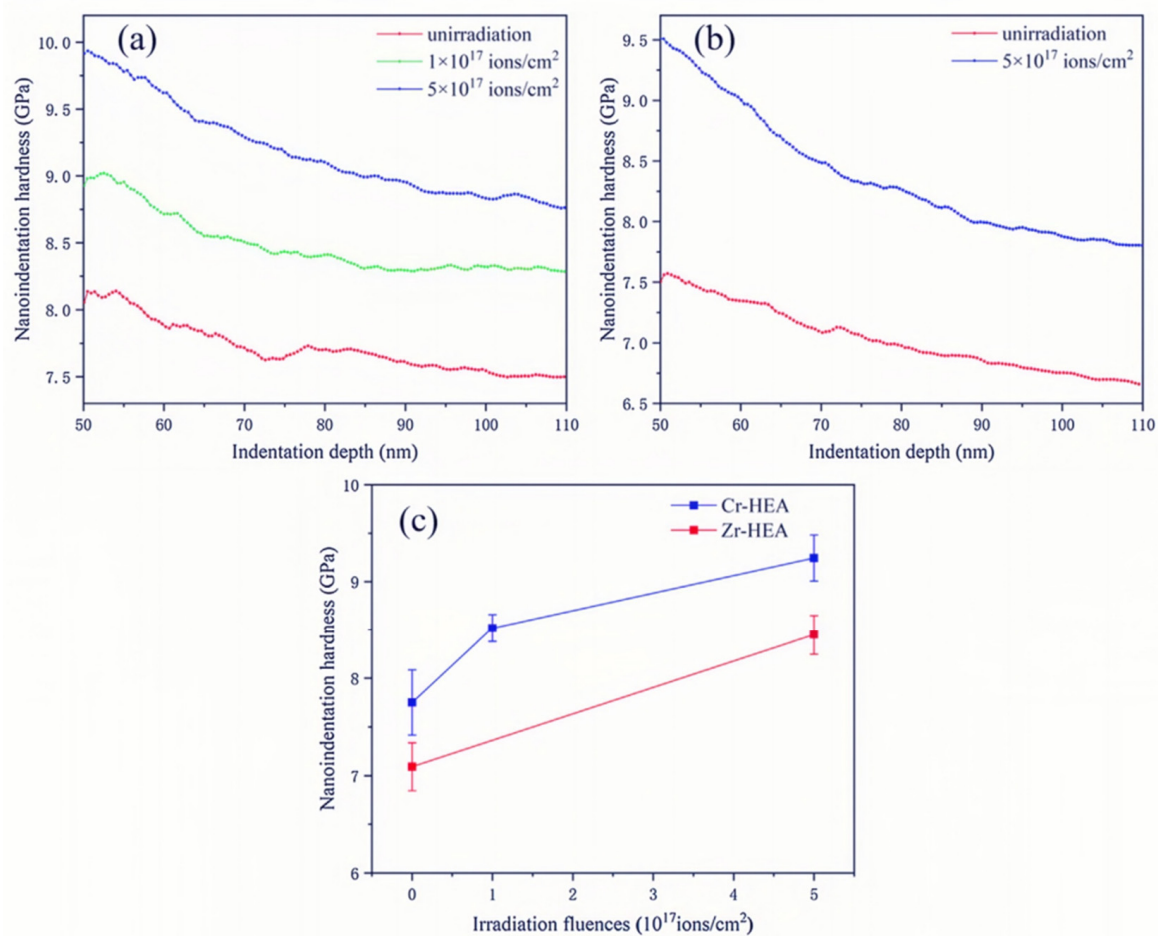
Figure 16. (**a**) nanoindentation hardness as a function of the indentation depth in the unirradiated and irradiated Cr-HEA at ion fluences of 1×10^{17} ions/cm^2 and 5×10^{17} ions/cm^2. (**b**) nanoindentation hardness as a function of the indentation depth in the unirradiated and irradiated Zr-HEA at ion fluences of 5×10^{17} ions/cm^2. (**c**) average nanoindentation hardness as a function of the irradiation fluence in the unirradiated and irradiated Cr-HEA and Zr-HEA (Reprinted with permission from ref. [126]. Copyright 2017 Elsevier.).

4. High-Throughput Techniques

Because of the multi-component characteristics of HEAs, the number of HEA compositions is increasing rapidly. Traditional methods are impractical to achieve synthesis, characterization, modeling and optimization of HEAs' compositions.

To explore the huge compositional spaces and more effectively improve the alloy development, high-throughput calculation techniques have been put forward, overcoming the time-consuming and laborious nature of traditional experiments [127]. Bulk samples of freely chosen compositions can be produced by high-throughput synthesis techniques, to achieve microstructures closer to industrial demand. At present, high-throughput technology mainly includes empirical models, first-principle calculations, the calculation of phase diagrams (CALPHAD) and machine learning.

For example, Melia et al. [56] discussed the implications of high-throughput synthesis techniques and the coupling of high-throughput characterization and modeling techniques by preparing MoNbTaW with different numbers of components (i.e., MoNbTa graded to pure W, MoTaW graded to pure Nb and so on). Michael et al. [52] processed and characterized a wide range of compositions based on the MoNbTaW material system, including both equiatomic and nonequiatomic alloys. They proposed a method for rapid screening of complex, concentrated alloys by a combination of metal additive manufacturing, microscopy and high-throughput mechanical testing. The samples exhibited a propensity for brittle

fracture or cracking, likely due to the intrinsically low workability of these alloys, and mitigation strategies to avoid cracking were discussed. Light, strong and low-cost AlCrFeMnTi HEAs for elevated-temperature applications were designed by a CALPHAD-based high-throughput computational method [128]. Precipitation-strengthened AlCrFeMnTi HEAs, which were selected from thousands of initial compositions, exhibit enhanced strength compared to their counterparts at room and elevated temperatures (flowchart is shown in Figure 17).
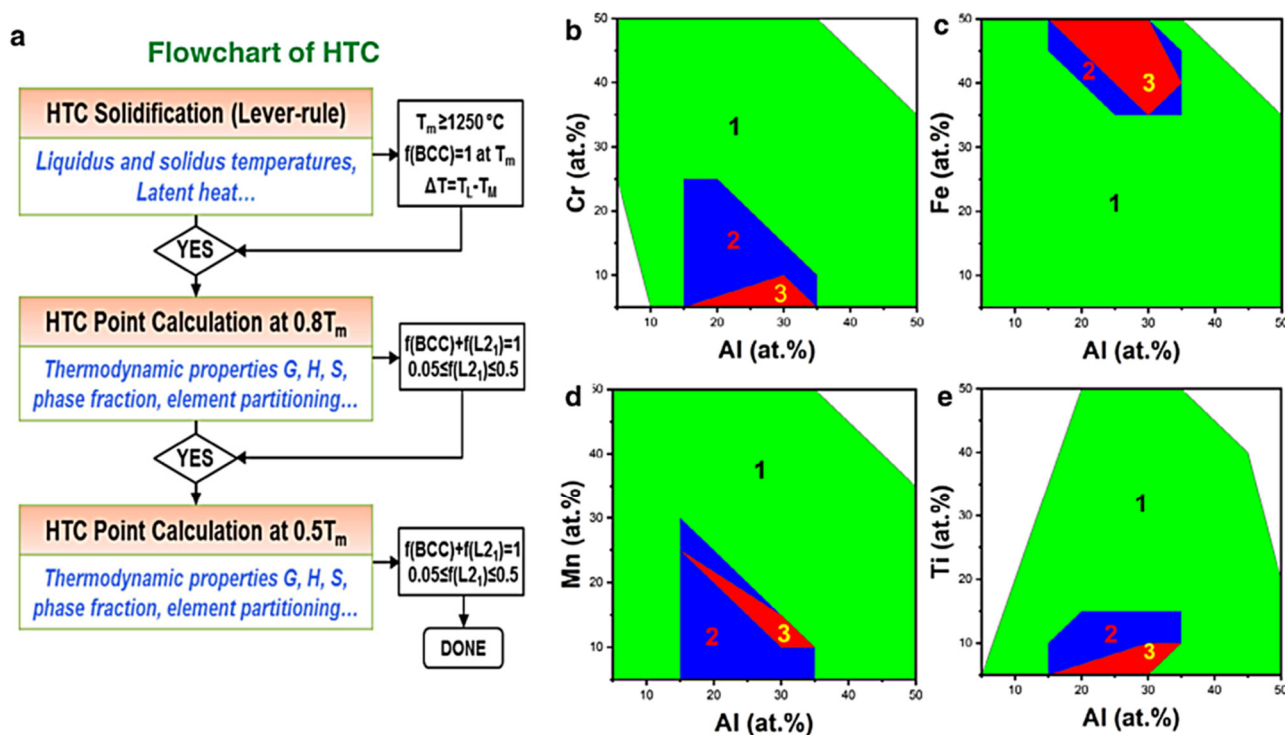

Figure 17. High-throughput screening of optimal alloy compositions in the Al–Cr–Fe–Mn–Ti system: (**a**) Flowchart of the current HTC, (**b**) Al–Cr projection, (**c**) Al–Fe projection, (**d**) Al–Mn projection and (**e**) Al–Ti projection (Reprinted from ref. [128]).

These cases show that high-throughput processing and characterization can enable rapid screening of complex, concentrated HEAs and their optimization for structural applications.

5. Summary and Outlook

This paper reviewed all aspects involved in the field of HEAs with a BCC structure. We compared the mechanical properties of BCC HEAs prepared by vacuum arc-melting, powder metallurgy (mainly MA with SPS) and additive manufacturing (mainly DLD). At present, BCC HEAs with high specific strength and reasonable ductility are prepared by vacuum arc-melting, which is also the most mature and widely used preparation technology. Moreover, the samples prepared by PM exhibited better properties owing to their ultrafine grains, excellent microstructural homogeneity, improved strength and hardness. PM is a promising way to prepare ductile RHEAs with outstanding comprehensive mechanical properties. The development of AM technology is promoted by new materials exploitation and structural optimization. The samples with refined microstructure are mainly attributed to the success of the rapid solidification in the AM preparation process. It is possible to prepare HEA products with complex geometry that can be used in aerospace, energy, molding, tooling and other industries by AM. However, relevant studies on AM are limited at present and the simultaneous handling of several elemental or pre-alloyed powders brings new challenges to the deposition process of AM. The influence of HEAs property

(atomic size difference, mixing entropy, mixing enthalpy, valence electron concentration, electronegativity difference, etc.), processing technique (DED, SLM, EBM, etc.), process parameters (laser/electron beam power, scanning speed, scanning pitch, layer thickness, etc.) on mechanical properties (strength, ductility, fatigue life, wear resistance, etc.) of printed HEA products should be considered simultaneously, rather than just some of them. It is hoped that more experts will pay attention to BCC high entropy alloys and improve the relevant research mentioned above, thereby refining their applicability in a broad range of industries.

As an important part of BCC HEAs, the high-temperature properties of RHEAs have also attracted extensive attention. In addition to the preparation process, alloying also plays a great role in the improvement of mechanical properties. For instance, Ti can facilitate grain refinement, Cr can promote Laves phase precipitated in the BCC matrix and Al can trigger the appearance of the BCC2 phase. It has been studied that Al, Cr and Si addition can improve the high-temperature oxidation resistance of RHEAs. However, unfortunately, this approach worsens room-temperature ductility. How to improve the oxidation resistance of RHEAs while achieving optimal room temperature ductility seems to be a challenge.

At present, the research on high entropy alloys, especially BCC high entropy alloys, is still in the initial stage, and the formation mechanism of its single solid solution is not perfect. In addition, the composition design of high-entropy alloys has great flexibility. The high-throughput method can effectively screen new high-entropy alloys and rapidly prepare high-entropy alloys with different components, thus improving the development speed of high-entropy alloys and overcoming the traditional characteristics of time-consuming and laborious experiments.

Overall, most BCC-structured HEAs display good mechanical properties, especially for RHEAs at high temperatures, common systems and applications are listed in Table 1.

Table 1. Common systems and applications.

Alloy System	Applications	Reference
TiAlFeCoNi	Biomedical materials	[73]
TiZrNbTaMo	Biomedical materials	[117]
$Mo_{0.5}NbTiV_{0.5}Zr_{0.25}$	Radiation resistant material	[121]
CrMoNbV	Aviation Materials	[129]
$Zr_{45}Ti_{31.5}Nb_{13.5}Al_{10}$	Aviation Materials	[130]

In biomedical applications, TiAlFeCoNi HEA exhibited 170~580% higher hardness, low elastic modulus and 260~1020% better cellular metabolic activity compared to titanium and Ti-6Al-7Nb biomaterials. The TiZrNbTaMo HEA possesses Young's modulus of 153 GPa, Vickers microhardness of 4.9 GPa, excellent compressive properties (σy = 1390 MPa and $\varepsilon p \approx 6\%$). Besides, it exhibited excellent corrosion resistance in PBS and was remarkably superior to the 316LSS and CoCrMo alloys. Those HEAs confirm the high potential for future biomedical applications. In nuclear applications, $Mo_{0.5}NbTiVCr_{0.25}$ shows slight irradiation hardening compared with most of the conventional alloys and shows outstanding irradiation resistance, which may be promising accident-tolerant fuel cladding materials. In aviation materials, The CrMoNbV has superior high temperature strength, attributed to the large atomic-size and elastic-modulus mismatches, the insensitive temperature dependence of elastic properties, and the dominance of non-screw character dislocations. Furthermore, $Zr_{45}Ti_{31.5}Nb_{13.5}Al_{10}$ HEA is a novel ultra-strong (1.2 GPa) and tough (~25%) alloy with low density. These HEAs have potential as aerospace materials.

However, so far, research on the high temperature fatigue properties, creep properties and high temperature oxidation properties of BCC HEAs is not extensive. The successful application of a new alloy in the industry requires a comprehensive performance test and in-depth evaluation. Therefore, there is still a long way to go in the research of BCC HEAs. The industrialization of BCC HEAs still faces great challenges.

Institutional Review Board Statement: Not applicable.

Informed Consent Statement: Not applicable.

Data Availability Statement: All data included in this study are available from the corresponding author on reasonable request.

Conflicts of Interest: The authors declare no conflict of interest.

References

1. Yeh, J.-W. Recent progress in high-entropy alloys. *Ann. Chim. Sci. Mat* **2006**, *31*, 633–648. [CrossRef]
2. Chang, Y.-J.; Yeh, A.-C. The evolution of microstructures and high temperature properties of $Al_xCo_{1.5}CrFeNi_{1.5}Ti_y$ high entropy alloys. *J. Alloys Compd.* **2015**, *653*, 379–385. [CrossRef]
3. Gludovatz, B.; Hohenwarter, A.; Catoor, D.; Chang, E.H.; George, E.P.; Ritchie, R.O. A fracture-resistant high-entropy alloy for cryogenic applications. *Science* **2014**, *345*, 1153–1158. [CrossRef] [PubMed]
4. Chuang, M.-H.; Tsai, M.-H.; Wang, W.-R.; Lin, S.-J.; Yeh, J.-W. Microstructure and wear behavior of $Al_xCo_{1.5}CrFeNi_{1.5}Ti_y$ high-entropy alloys. *Acta Mater.* **2011**, *59*, 6308–6317. [CrossRef]
5. Chen, J.; Niu, P.; Liu, Y.; Lu, Y.; Wang, X.; Peng, Y.; Liu, J. Effect of Zr content on microstructure and mechanical properties of AlCoCrFeNi high entropy alloy. *Mater. Des.* **2016**, *94*, 39–44. [CrossRef]
6. Cheng, K.-H.; Lai, C.-H.; Lin, S.-J.; Yeh, J.-W. Structural and mechanical properties of multi-element $(AlCrMoTaTiZr)N_x$ coatings by reactive magnetron sputtering. *Thin Solid Films* **2011**, *519*, 3185–3190. [CrossRef]
7. Daoud, H.M.; Manzoni, A.M.; Wanderka, N.; Glatzel, U. High-Temperature Tensile Strength of $Al_{10}Co_{25}Cr_8Fe_{15}Ni_{36}Ti_6$ Compositionally Complex Alloy (High-Entropy Alloy). *JOM* **2015**, *67*, 2271–2277. [CrossRef]
8. Fu, Z.; Yang, B.; Gan, K.; Yan, D.; Li, Z.; Gou, G.; Chen, H.; Wang, Z. Improving the hydrogen embrittlement resistance of a selective laser melted high-entropy alloy via modifying the cellular structures. *Corros. Sci.* **2021**, *190*, 109695. [CrossRef]
9. Chen, Y.Y.; Duval, T.; Hung, U.D.; Yeh, J.W.; Shih, H.C. Microstructure and electrochemical properties of high entropy alloys—a comparison with type-304 stainless steel. *Corros. Sci.* **2005**, *47*, 2257–2279. [CrossRef]
10. Chen, Y.Y.; Hong, U.T.; Shih, H.C.; Yeh, J.W.; Duval, T. Electrochemical kinetics of the high entropy alloys in aqueous environments—a comparison with type 304 stainless steel. *Corros. Sci.* **2005**, *47*, 2679–2699. [CrossRef]
11. Quiambao, K.F.; McDonnell, S.J.; Schreiber, D.K.; Gerard, A.Y.; Freedy, K.M.; Lu, P.; Saal, J.E.; Frankel, G.S.; Scully, J.R. Passivation of a corrosion resistant high entropy alloy in non-oxidizing sulfate solutions. *Acta Mater.* **2019**, *164*, 362–376. [CrossRef]
12. Cantor, B.; Chang, I.; Knight, P.; Vincent, A. Microstructural development in equiatomic multicomponent alloys. *Mater. Sci. Eng. A* **2004**, *375–377*, 213–218. [CrossRef]
13. Senkov, O.N.; Wilks, G.B.; Miracle, D.B.; Chuang, C.P.; Liaw, P.K. Refractory high-entropy alloys. *Intermetallics* **2010**, *18*, 1758–1765. [CrossRef]
14. Takeuchi, A.; Amiya, K.; Wada, T.; Yubuta, K.; Zhang, W. High-Entropy Alloys with a Hexagonal Close-Packed Structure Designed by Equi-Atomic Alloy Strategy and Binary Phase Diagrams. *JOM* **2014**, *66*, 1984–1992. [CrossRef]
15. Gao, M.C.; Zhang, B.; Guo, S.M.; Qiao, J.W.; Hawk, J.A. High-Entropy Alloys in Hexagonal Close-Packed Structure. *Metall. Mater. Trans. A* **2016**, *47*, 3322–3332. [CrossRef]
16. Zhang, Y.; Li, R. New Advances in High-Entropy Alloys. *Entropy* **2020**, *22*, 1158. [CrossRef]
17. Zhang, Y.; Ai, Y.; Chen, W.; Ouyang, S. Preparation and microstructure and properties of AlCuFeMnTiV lightweight high entropy alloy. *J. Alloys Compd.* **2022**, *900*, 163352. [CrossRef]
18. Fu, X.; Schuh, C.A.; Olivetti, E.A. Materials selection considerations for high entropy alloys. *Scr. Mater.* **2017**, *138*, 145–150. [CrossRef]
19. Waseem, O.A.; Ryu, H.J. Powder Metallurgy Processing of a $W_xTaTiVCr$ High-Entropy Alloy and Its Derivative Alloys for Fusion Material Applications. *Sci. Rep.* **2017**, *7*, 1926. [CrossRef]
20. Wu, Y.D.; Cai, Y.H.; Wang, T.; Si, J.J.; Zhu, J.; Wang, Y.D.; Hui, X.D. A refractory $Hf_{25}Nb_{25}Ti_{25}Zr_{25}$ high-entropy alloy with excellent structural stability and tensile properties. *Mater. Lett.* **2014**, *130*, 277–280. [CrossRef]

21. Yao, H.; Tan, Z.; He, D.; Zhou, Z.; Zhou, Z.; Xue, Y.; Cui, L.; Chen, L.; Wang, G.; Yang, Y. High strength and ductility AlCrFeNiV high entropy alloy with hierarchically heterogeneous microstructure prepared by selective laser melting. *J. Alloys Compd.* **2020**, *813*, 152196. [CrossRef]

22. Son, S.; Kim, S.; Kwak, J.; Gu, G.H.; Hwang, D.S.; Kim, Y.-T.; Kim, H.S. Superior antifouling properties of a CoCrFeMnNi high-entropy alloy. *Mater. Lett.* **2021**, *300*, 130130. [CrossRef]

23. Xia, S.; Xia, Z.; Zhao, D.; Xie, Y.; Liu, X.; Wang, L. Microstructure formation mechanism and corrosion behavior of FeCrCuTiV two-phase high entropy alloy prepared by different processes. *Fusion Eng. Des.* **2021**, *172*, 112792. [CrossRef]

24. Avila-Rubio, M.A.; Carreño-Gallardo, C.; Herrera-Ramirez, J.M.; García-Grajeda, B.A.; Pérez-González, F.A.; Ramirez-Ramirez, J.H.; Garza-Montes-de-Oca, N.F.; Baldenebro-Lopez, F.J. Microstructure and microhardness of high entropy alloys with Zn addition: AlCoFeNiZn and AlCoFeNiMoTiZn. *Adv. Powder Technol.* **2021**, *32*, 4687–4696. [CrossRef]

25. Ye, Q.; Yang, B.; Yang, G.; Zhao, J.; Gong, Z. Stability prediction of AlCoCrFeMo$_{0.05}$Ni$_2$ high entropy alloy by Kinetic Monte Carlo method. *Mater. Lett.* **2022**, *306*, 130907. [CrossRef]

26. Daryoush, S.; Mirzadeh, H.; Ataie, A. Amorphization, mechano-crystallization, and crystallization kinetics of mechanically alloyed AlFeCuZnTi high-entropy alloys. *Mater. Lett.* **2022**, *307*, 131098. [CrossRef]

27. Wang, Y.P.; Li, B.S.; Ren, M.X.; Yang, C.; Fu, H.Z. Microstructure and compressive properties of AlCrFeCoNi high entropy alloy. *Mater. Sci. Eng. A* **2008**, *491*, 154–158. [CrossRef]

28. Zhang, L.J.; Jiang, Z.K.; Zhang, M.D.; Fan, J.T.; Liu, D.J.; Yu, P.F.; Liu, R.P. Effect of solid carburization on the surface microstructure and mechanical properties of the equiatomic CoCrFeNi high-entropy alloy. *J. Alloys Compd.* **2018**, *769*, 27–36. [CrossRef]

29. Nishimoto, A.; Fukube, T.; Maruyama, T. Microstructural, mechanical, and corrosion properties of plasma-nitrided CoCrFeMnNi high-entropy alloys. *Surf. Coat. Technol.* **2018**, *376*, 52–58. [CrossRef]

30. Günen, A. Tribocorrosion behavior of boronized Co$_{1.19}$Cr$_{1.86}$Fe$_{1.30}$Mn$_{1.39}$Ni$_{1.05}$Al$_{0.17}$B$_{0.04}$ high entropy alloy. *Surf. Coat. Technol.* **2021**, *421*, 127426. [CrossRef]

31. Karakaş, M.S.; Günen, A.; Çarboğa, C.; Karaca, Y.; Demir, M.; Altınay, Y.; Erdoğan, A. Microstructure, some mechanical properties and tribocorrosion wear behavior of boronized Al$_{0.07}$Co$_{1.26}$Cr$_{1.80}$Fe$_{1.42}$Mn$_{1.35}$Ni$_{1.10}$ high entropy alloy. *J. Alloys Compd.* **2021**, *886*, 161222. [CrossRef]

32. Scales, R.J.; Armstrong, D.; Wilkinson, A.J.; Li, B.-S. On the brittle-to-ductile transition of the as-cast TiVNbTa refractory high-entropy alloy. *Materialia* **2020**, *14*, 100940. [CrossRef]

33. Wang, M.; Ma, Z.; Xu, Z.; Cheng, X. Microstructures and mechanical properties of HfNbTaTiZrW and HfNbTaTiZrMoW refractory high-entropy alloys. *J. Alloys Compd.* **2019**, *803*, 778–785. [CrossRef]

34. Wang, M.; Ma, Z.L.; Xu, Z.Q.; Cheng, X.W. Designing V NbMoTa refractory high-entropy alloys with improved properties for high-temperature applications. *Scr. Mater.* **2021**, *191*, 131–136. [CrossRef]

35. Guo, W.; Liu, B.; Liu, Y.; Li, T.; Fu, A.; Fang, Q.; Nie, Y. Microstructures and mechanical properties of ductile NbTaTiV refractory high entropy alloy prepared by powder metallurgy. *J. Alloys Compd.* **2019**, *776*, 428–436. [CrossRef]

36. Praveen, S.; Basu, J.; Kashyap, S.; Kottada, R.S. Exceptional resistance to grain growth in nanocrystalline CoCrFeNi high entropy alloy at high homologous temperatures. *J. Alloys Compd.* **2016**, *662*, 361–367. [CrossRef]

37. Kang, B.; Kong, T.; Ryu, H.J.; Hong, S.H. Superior mechanical properties and strengthening mechanisms of lightweight Al$_x$CrNbVMo refractory high-entropy alloys (x = 0, 0.5, 1.0) fabricated by the powder metallurgy process. *J. Mater. Sci. Technol.* **2021**, *69*, 32–41. [CrossRef]

38. Cao, Y.; Liu, Y.; Liu, B.; Zhang, W. Precipitation behavior during hot deformation of powder metallurgy Ti-Nb-Ta-Zr-Al high entropy alloys. *Intermetallics* **2018**, *100*, 95–103. [CrossRef]

39. Ostovari Moghaddam, A.; Shaburova, N.A.; Samodurova, M.N.; Abdollahzadeh, A.; Trofimov, E.A. Additive manufacturing of high entropy alloys: A practical review. *J. Mater. Sci. Technol.* **2021**, *77*, 131–162. [CrossRef]

40. Kranz, J.; Herzog, D.; Emmelmann, C. Design guidelines for laser additive manufacturing of lightweight structures in TiAl$_6$V$_4$. *J. Laser Appl.* **2015**, *27*, S14001. [CrossRef]

41. Li, N.; Huang, S.; Zhang, G.; Qin, R.; Liu, W.; Xiong, H.; Shi, G.; Blackburn, J. Progress in additive manufacturing on new materials: A review. *J. Mater. Sci. Technol.* **2019**, *35*, 242–269. [CrossRef]

42. Huang, H.; Wu, Y.; He, J.; Wang, H.; Liu, X.; An, K.; Wu, W.; Lu, Z. Phase-Transformation Ductilization of Brittle High-Entropy Alloys via Metastability Engineering. *Adv. Mater.* **2017**, *29*, 1701678. [CrossRef] [PubMed]

43. Popov, V.V.; Katz-Demyanetz, A.; Koptyug, A.; Bamberger, M. Selective electron beam melting of Al$_{0.5}$CrMoNbTa$_{0.5}$ high entropy alloys using elemental powder blend. *Heliyon* **2019**, *5*, e01188. [CrossRef] [PubMed]

44. Senkov, O.N.; Miracle, D.B.; Chaput, K.J.; Couzinie, J.-P. Development and exploration of refractory high entropy alloys—A review. *J. Mater. Res.* **2018**, *33*, 3092–3128. [CrossRef]

45. Zhang, H.; Zhao, Y.; Huang, S.; Zhu, S.; Wang, F.; Li, D. Manufacturing and Analysis of High-Performance Refractory High-Entropy Alloy via Selective Laser Melting (SLM). *Materials* **2019**, *12*, 720. [CrossRef] [PubMed]

46. Cao, B.X.; Yang, T.; Fan, L.; Luan, J.H.; Jiao, Z.B.; Liu, C.T. Refractory alloying additions on the thermal stability and mechanical properties of high-entropy alloys. *Mater. Sci. Eng. A* **2020**, *797*, 140020. [CrossRef]

47. Panina, E.S.; Yurchenko, N.; Zherebtsov, S.V.; Tikhonovsky, M.A.; Mishunin, M.V.; Stepanov, N.D. Structures and mechanical properties of Ti-Nb-Cr-V-Ni-Al refractory high entropy alloys. *Mater. Sci. Eng. A* **2020**, *786*, 139409. [CrossRef]

48. Lu, S.; Li, X.; Liang, X.; Yang, W.; Chen, J. Effect of V and Ti on the Oxidation Resistance of WMoTaNb Refractory High-Entropy Alloy at High Temperatures. *Metals* **2022**, *12*, 41. [CrossRef]

49. Müller, F.; Gorr, B.; Christ, H.-J.; Müller, J.; Butz, B.; Chen, H.; Kauffmann, A.; Heilmaier, M. On the oxidation mechanism of refractory high entropy alloys. *Corros. Sci.* **2019**, *159*, 108161. [CrossRef]

50. Fu, Y.; Li, J.; Luo, H.; Du, C.; Li, X. Recent advances on environmental corrosion behavior and mechanism of high-entropy alloys. *J. Mater. Sci. Technol.* **2021**, *80*, 217–233. [CrossRef]

51. Jensen, J.K.; Welk, B.A.; Williams, R.; Sosa, J.M.; Huber, D.E.; Senkov, O.N.; Viswanathan, G.B.; Fraser, H.L. Characterization of the microstructure of the compositionally complex alloy Al1Mo$_{0.5}$Nb$_1$Ta$_{0.5}$Ti$_1$Zr$_1$. *Scr. Mater.* **2016**, *121*, 1–4. [CrossRef]

52. Melia, M.A.; Whetten, S.R.; Puckett, R.; Jones, M.; Heiden, M.J.; Argibay, N.; Kustas, A.B. High-throughput additive manufacturing and characterization of refractory high entropy alloys. *Appl. Mater. Today* **2020**, *19*, 100560. [CrossRef]

53. Moorehead, M.; Bertsch, K.; Niezgoda, M.; Parkin, C.; Elbakhshwan, M.; Sridharan, K.; Zhang, C.; Thoma, D.; Couet, A. High-throughput synthesis of Mo-Nb-Ta-W high-entropy alloys via additive manufacturing. *Mater. Des.* **2020**, *187*, 108358. [CrossRef]

54. Xia, S.Q.; Yang, X.; Yang, T.F.; Liu, S.; Zhang, Y. Irradiation resistance in Al$_x$CoCrFeNi high entropy alloys. *JOM* **2015**, *67*, 2340–2344. [CrossRef]

55. Xia, S.Q.; Wang, Z.; Yang, T.F.; Zhang, Y. Irradiation Behavior in High Entropy Alloys. *J. Iron Steel Res. Int.* **2015**, *22*, 879–884. [CrossRef]

56. George, E.P.; Curtin, W.A.; Tasan, C.C. High entropy alloys: A focused review of mechanical properties and deformation mechanisms. *Acta Mater.* **2020**, *188*, 435–474. [CrossRef]

57. Senkov, O.N.; Wilks, G.B.; Scott, J.M.; Miracle, D.B. Mechanical properties of Nb$_{25}$Mo$_{25}$Ta$_{25}$W$_{25}$ and V$_{20}$Nb$_{20}$Mo$_{20}$Ta$_{20}$W$_{20}$ refractory high entropy alloys. *Intermetallics* **2011**, *19*, 698–706. [CrossRef]

58. Zhang, B.; Gao, M.C.; Zhang, Y.; Yang, S.; Guo, S.M. Senary refractory high entropy alloy MoNbTaTiVW. *Mater. Sci. Technol.* **2015**, *31*, 1207–1213. [CrossRef]

59. Senkov, O.N.; Scott, J.M.; Senkova, S.V.; Meisenkothen, F.; Miracle, D.B.; Woodward, C.F. Microstructure and elevated temperature properties of a refractory TaNbHfZrTi alloy. *J. Mater. Sci.* **2012**, *47*, 4062–4074. [CrossRef]

60. Senkov, O.N.; Senkova, S.V.; Miracle, D.B.; Woodward, C. Mechanical properties of low-density, refractory multi-principal element alloys of the Cr–Nb–Ti–V–Zr system. *Mater. Sci. Eng. A* **2013**, *565*, 51–62. [CrossRef]

61. Senkov, O.N.; Senkova, S.V.; Woodward, C. Effect of aluminum on the microstructure and properties of two refractory high-entropy alloys. *Acta Mater.* **2014**, *68*, 214–228. [CrossRef]

62. Couzinié, J.P.; Dirras, G.; Perrière, L.; Chauveau, T.; Leroy, E.; Champion, Y.; Guillot, I. Microstructure of a near-equimolar refractory high-entropy alloy. *Mater. Lett.* **2014**, *126*, 285–287. [CrossRef]

63. Senkov, O.N.; Scott, J.M.; Senkova, S.V.; Miracle, D.B.; Woodward, C.F. Microstructure and room temperature properties of a high-entropy TaNbHfZrTi alloy. *J. Alloys Compd.* **2011**, *509*, 6043–6048. [CrossRef]

64. Senkov, O.N.; Senkova, S.V.; Woodward, C.; Miracle, D.B. Low-density, refractory multi-principal element alloys of the Cr–Nb–Ti–V–Zr system: Microstructure and phase analysis. *Acta Mater.* **2013**, *61*, 1545–1557. [CrossRef]

65. Fazakas, É.; Zadorozhnyy, V.; Varga, L.K.; Inoue, A.; Louzguine-Luzgin, D.V.; Tian, F.; Vitos, L. Experimental and theoretical study of Ti$_{20}$Zr$_{20}$Hf$_{20}$Nb$_{20}$X$_{20}$ (X=V or Cr) refractory high-entropy alloys. *Int. J. Refract. Met. Hard Mater.* **2014**, *47*, 131–138. [CrossRef]

66. Poletti, M.G.; Fiore, G.; Szost, B.A.; Battezzati, L. Search for high entropy alloys in the X-NbTaTiZr systems (X=Al, Cr, V, Sn). *J. Alloys Compd.* **2015**, *620*, 283–288. [CrossRef]

67. Stepanov, N.D.; Shaysultanov, D.G.; Salishchev, G.A.; Tikhonovsky, M.A. Structure and mechanical properties of a light-weight AlNbTiV high entropy alloy. *Mater. Lett.* **2015**, *142*, 153–155. [CrossRef]

68. Yao, H.W.; Qiao, J.W.; Gao, M.C.; Hawk, J.A.; Ma, S.G.; Zhou, H.F.; Zhang, Y. NbTaV-(Ti,W) refractory high-entropy alloys: Experiments and modeling. *Mater. Sci. Eng. A* **2016**, *674*, 203–211. [CrossRef]

69. Liao, M.; Liu, Y.; Min, L.; Lai, Z.; Han, T.; Yang, D.; Zhu, J. Alloying effect on phase stability, elastic and thermodynamic properties of Nb-Ti-V-Zr high entropy alloy. *Intermetallics* **2018**, *101*, 152–164. [CrossRef]

70. King, D.; Cheung, S.; Humphry-Baker, S.A.; Parkin, C.; Couet, A.; Cortie, M.B.; Lumpkin, G.R.; Middleburgh, S.C.; Knowles, A.J. High temperature, low neutron cross-section high-entropy alloys in the Nb-Ti-V-Zr system. *Acta Mater.* **2019**, *166*, 435–446. [CrossRef]

71. Liao, M.; Liu, Y.; Cui, P.; Qu, N.; Zhou, F.; Yang, D.; Han, T.; Lai, Z.; Zhu, J. Modeling of alloying effect on elastic properties in BCC Nb-Ti-V-Zr solid solution: From unary to quaternary. *Comput. Mater. Sci.* **2020**, *172*, 109289. [CrossRef]

72. Zou, Y.; Maiti, S.; Steurer, W.; Spolenak, R. Size-dependent plasticity in an Nb$_{25}$Mo$_{25}$Ta$_{25}$W$_{25}$ refractory high-entropy alloy. *Acta Mater.* **2014**, *65*, 85–97. [CrossRef]

73. Han, Z.D.; Chen, N.; Zhao, S.F.; Fan, L.W.; Yang, G.N.; Shao, Y.; Yao, K.F. Effect of Ti additions on mechanical properties of NbMoTaW and VNbMoTaW refractory high entropy alloys. *Intermetallics* **2017**, *84*, 153–157. [CrossRef]

74. Joo, S.-H.; Kato, H.; Jang, M.J.; Moon, J.; Kim, E.B.; Hong, S.-J.; Kim, H.S. Structure and properties of ultrafine-grained CoCrFeMnNi high-entropy alloys produced by mechanical alloying and spark plasma sintering. *J. Alloys Compd.* **2017**, *698*, 591–604. [CrossRef]

75. Sathiyamoorthi, P.; Basu, J.; Kashyap, S.; Pradeep, K.G.; Kottada, R.S. Thermal stability and grain boundary strengthening in ultrafine-grained CoCrFeNi high entropy alloy composite. *Mater. Des.* **2017**, *134*, 426–433. [CrossRef]

76. Wang, P.; Cai, H.; Zhou, S.; Xu, L. Processing, microstructure and properties of $Ni_{1.5}CoCuFeCr_{0.5-x}V_x$ high entropy alloys with carbon introduced from process control agent. *J. Alloys Compd.* **2017**, *695*, 462–475. [CrossRef]

77. Pan, J.; Dai, T.; Lu, T.; Ni, X.; Dai, J.; Li, M. Microstructure and mechanical properties of $Nb_{25}Mo_{25}Ta_{25}W_{25}$ and $Ti_8Nb_{23}Mo_{23}Ta_{23}W_{23}$ high entropy alloys prepared by mechanical alloying and spark plasma sintering. *Mater. Sci. Eng. A* **2018**, *738*, 362–366. [CrossRef]

78. Zhang, Y.; Qiao, J.; Liaw, P.K. A Brief Review of High Entropy Alloys and Serration Behavior and Flow Units. *J. Iron Steel Res. Int.* **2016**, *23*, 2–6. [CrossRef]

79. Kang, B.; Lee, J.; Ryu, H.J.; Hong, S.H. Ultra-high strength WNbMoTaV high-entropy alloys with fine grain structure fabricated by powder metallurgical process. *Mater. Sci. Eng. A* **2018**, *712*, 616–624. [CrossRef]

80. Long, Y.; Liang, X.; Su, K.; Peng, H.; Li, X. A fine-grained NbMoTaWVCr refractory high-entropy alloy with ultra-high strength: Microstructural evolution and mechanical properties. *J. Alloys Compd.* **2019**, *780*, 607–617. [CrossRef]

81. Senkov, O.N.; Woodward, C.F. Microstructure and properties of a refractory $NbCrMo_{0.5}Ta_{0.5}TiZr$ alloy. *Mater. Sci. Eng. A* **2011**, *529*, 311–320. [CrossRef]

82. Prieto, E.; de Oro Calderon, R.; Konegger, T.; Gordo, E.; Gierl-Mayer, C.; Sheikh, S.; Guo, S.; Danninger, H.; Milenkovic, S.; Alvaredo, P. Processing of a new high entropy alloy: AlCrFeMoNiTi. *Powder Metall.* **2018**, *61*, 258–265. [CrossRef]

83. Koundinya, N.T.B.N.; Sajith Babu, C.; Sivaprasad, K.; Susila, P.; Kishore Babu, N.; Baburao, J. Phase Evolution and Thermal Analysis of Nanocrystalline AlCrCuFeNiZn High Entropy Alloy Produced by Mechanical Alloying. *J. Mater. Eng. Perform.* **2013**, *22*, 3077–3084. [CrossRef]

84. Varalakshmi, S.; Kamaraj, M.; Murty, B.S. Synthesis and characterization of nanocrystalline AlFeTiCrZnCu high entropy solid solution by mechanical alloying. *J. Alloys Compd.* **2008**, *460*, 253–257. [CrossRef]

85. Waseem, O.A.; Lee, J.; Lee, H.M.; Ryu, H.J. The effect of Ti on the sintering and mechanical properties of refractory high-entropy alloy $Ti_xWTaVCr$ fabricated via spark plasma sintering for fusion plasma-facing materials. *Mater. Chem. Phys.* **2018**, *210*, 87–94. [CrossRef]

86. Song, R.; Wei, L.; Yang, C.; Wu, S. Phase formation and strengthening mechanisms in a dual-phase nanocrystalline CrMnFeVTi high-entropy alloy with ultrahigh hardness. *J. Alloys Compd.* **2018**, *744*, 552–560. [CrossRef]

87. Raza, A.; Kang, B.; Lee, J.; Ryu, H.J.; Hong, S.H. Transition in microstructural and mechanical behavior by reduction of sigma-forming element content in a novel high entropy alloy. *Mater. Des.* **2018**, *145*, 11–19. [CrossRef]

88. Raza, A.; Ryu, H.J.; Hong, S.H. Strength enhancement and density reduction by the addition of Al in CrFeMoV based high-entropy alloy fabricated through powder metallurgy. *Mater. Des.* **2018**, *157*, 97–104. [CrossRef]

89. Dobbelstein, H.; Thiele, M.; Gurevich, E.L.; George, E.P.; Ostendorf, A. Direct Metal Deposition of Refractory High Entropy Alloy MoNbTaW. *Phys. Procedia* **2016**, *83*, 624–633. [CrossRef]

90. Dobbelstein, H.; Gurevich, E.L.; George, E.P.; Ostendorf, A.; Laplanche, G. Laser metal deposition of compositionally graded TiZrNbTa refractory high-entropy alloys using elemental powder blends. *Addit. Manuf.* **2019**, *25*, 252–262. [CrossRef]

91. Zhou, R.; Liu, Y.; Liu, B.; Li, J.; Fang, Q. Precipitation behavior of selective laser melted $FeCoCrNiC_{0.05}$ high entropy alloy. *Intermetallics* **2019**, *106*, 20–25. [CrossRef]

92. Xu, Z.; Zhang, H.; Li, W.; Mao, A.; Wang, L.; Song, G.; He, Y. Microstructure and nanoindentation creep behavior of CoCrFeMnNi high-entropy alloy fabricated by selective laser melting. *Addit. Manuf.* **2019**, *28*, 766–771. [CrossRef]

93. Park, J.M.; Choe, J.; Kim, J.G.; Bae, J.W.; Moon, J.; Yang, S.; Kim, K.T.; Yu, J.-H.; Kim, H.S. Superior tensile properties of 1%C-CoCrFeMnNi high-entropy alloy additively manufactured by selective laser melting. *Mater. Res. Lett.* **2020**, *8*, 1–7. [CrossRef]

94. Zhang, H.; Xu, W.; Xu, Y.; Lu, Z.; Li, D. The thermal-mechanical behavior of WTaMoNb high-entropy alloy via selective laser melting (SLM): Experiment and simulation. *Int. J. Adv. Manuf. Technol.* **2018**, *96*, 461–474. [CrossRef]

95. Wang, P.; Huang, P.; Ng, F.L.; Sin, W.J.; Lu, S.; Nai, M.L.S.; Dong, Z.; Wei, J. Additively manufactured CoCrFeNiMn high-entropy alloy via pre-alloyed powder. *Mater. Des.* **2019**, *168*, 107576. [CrossRef]

96. Shiratori, H.; Fujieda, T.; Yamanaka, K.; Koizumi, Y.; Kuwabara, K.; Kato, T.; Chiba, A. Relationship between the microstructure and mechanical properties of an equiatomic AlCoCrFeNi high-entropy alloy fabricated by selective electron beam melting. *Mater. Sci. Eng. A* **2016**, *656*, 39–46. [CrossRef]

97. Kuwabara, K.; Shiratori, H.; Fujieda, T.; Yamanaka, K.; Koizumi, Y.; Chiba, A. Mechanical and corrosion properties of AlCoCrFeNi high-entropy alloy fabricated with selective electron beam melting. *Addit. Manuf.* **2018**, *23*, 264–271. [CrossRef]

98. He, J.Y.; Liu, W.H.; Wang, H.; Wu, Y.; Liu, X.J.; Nieh, T.G.; Lu, Z.P. Effects of Al addition on structural evolution and tensile properties of the FeCoNiCrMn high-entropy alloy system. *Acta Mater.* **2014**, *62*, 105–113. [CrossRef]

99. Liu, X.-F.; Tian, Z.-L.; Zhang, X.-F.; Chen, H.-H.; Liu, T.-W.; Chen, Y.; Wang, Y.-J.; Dai, L.-H. "Self-sharpening" tungsten high-entropy alloy. *Acta Mater.* **2020**, *186*, 257–266. [CrossRef]

100. Zhou, X.; Li, S.; Liu, J.; Wang, Y.; Wang, X. Self-sharpening behavior during ballistic impact of the tungsten heavy alloy rod penetrators processed by hot-hydrostatic extrusion and hot torsion. *Mater. Sci. Eng. A* **2010**, *527*, 4881–4886. [CrossRef]

101. Li, Z.; Zhao, S.; Alotaibi, S.M.; Liu, Y.; Wang, B.; Meyers, M.A. Adiabatic shear localization in the CrMnFeCoNi high-entropy alloy. *Acta Mater.* **2018**, *151*, 424–431. [CrossRef]

102. Zener, C.; Hollomon, J.H. Effect of strain rate upon plastic flow of steel. *J. Appl. Phys.* **1944**, *15*, 22–32. [CrossRef]

103. Xue, Q.; Meyers, M.A.; Nesterenko, V.F. Self-organization of shear bands in titanium and Ti–6Al–4V alloy. *Acta Mater.* **2002**, *50*, 575–596. [CrossRef]

104. Khan, M.A.; Wang, Y.; Yasin, G.; Nazeer, F.; Malik, A.; Ahmad, T.; Khan, W.Q.; Nguyen, T.A.; Zhang, H.; Afifi, M.A. Adiabatic shear band localization in an Al–Zn–Mg–Cu alloy under high strain rate compression. *J. Mater. Res. Technol.* **2020**, *9*, 3977–3983. [CrossRef]

105. Boakye-Yiadom, S.; Bassim, N. Microstructural evolution of adiabatic shear bands in pure copper during impact at high strain rates. *Mater. Sci. Eng. A* **2018**, *711*, 182–194. [CrossRef]

106. Zhang, L.; Chen, X.; Huang, Y.; Liu, W.; Ma, Y. Microstructural characteristics and evolution mechanisms of 90W–Ni–Fe alloy under high-strain-rate deformation. *Mater. Sci. Eng. A* **2021**, *811*, 141070. [CrossRef]

107. Luo, R.; Huang, D.; Yang, M.; Tang, E.; Wang, M.; He, L. Penetrating performance and "self-sharpening" behavior of fine-grained tungsten heavy alloy rod penetrators. *Mater. Sci. Eng. A* **2016**, *675*, 262–270. [CrossRef]

108. Zhou, S.; Liang, Y.-J.; Zhu, Y.; Jian, R.; Wang, B.; Xue, Y.; Wang, L.; Wang, F. High entropy alloy: A promising matrix for high-performance tungsten heavy alloys. *J. Alloys Compd.* **2019**, *777*, 1184–1190. [CrossRef]

109. Upadhyaya, A. Processing strategy for consolidating tungsten heavy alloys for ordnance applications. *Mater. Chem. Phys.* **2001**, *67*, 101–110. [CrossRef]

110. Chen, H.-H.; Zhang, X.-F.; Dai, L.-H.; Liu, C.; Xiong, W.; Tan, M. Experimental study on WFeNiMo high-entropy alloy projectile penetrating semi-infinite steel target. *Def. Technol.* 2021, *in press*. [CrossRef]

111. Kim, B.G.; Kim, G.M.; Kim, C.J. Oxidation behavior of TiAl-X (X = Cr, V, Si, Mo or Nb) intermetallics at elevated temperature. *Scr. Metall. Mater.* **1995**, *33*, 1117–1125. [CrossRef]

112. Del Moricca, M.P.; Varma, S.K. High temperature oxidation characteristics of Nb–10W–XCr alloys. *J. Alloys Compd.* **2010**, *489*, 195–201. [CrossRef]

113. Zelenitsas, K.; Tsakiropoulos, P. Effect of Al, Cr and Ta additions on the oxidation behaviour of Nb–Ti–Si in situ composites at 800 °C. *Mater. Sci. Eng. A* **2006**, *416*, 269–280. [CrossRef]

114. Liu, C.M.; Wang, H.M.; Zhang, S.Q.; Tang, H.B.; Zhang, A.L. Microstructure and oxidation behavior of new refractory high entropy alloys. *J. Alloys Compd.* **2014**, *583*, 162–169. [CrossRef]

115. Qiu, Y.; Thomas, S.; Gibson, M.A.; Fraser, H.L.; Birbilis, N. Corrosion of high entropy alloys. *NPJ Mater. Degrad.* **2017**, *1*, 15. [CrossRef]

116. Shun, T.-T.; Du, Y.-C. Microstructure and tensile behaviors of FCC $Al_{0.3}$CoCrFeNi high entropy alloy. *J. Alloys Compd.* **2009**, *479*, 157–160. [CrossRef]

117. Wang, S.-P.; Xu, J. TiZrNbTaMo high-entropy alloy designed for orthopedic implants: As-cast microstructure and mechanical properties. *Mater. Sci. Eng. C Mater. Biol. Appl.* **2017**, *73*, 80–89. [CrossRef] [PubMed]

118. Hasegawa, A.; Fukuda, M.; Yabuuchi, K.; Nogami, S. Neutron irradiation effects on the microstructural development of tungsten and tungsten alloys. *J. Nucl. Mater.* **2016**, *471*, 175–183. [CrossRef]

119. Jenkins, M.; Kirk, M.; Phythian, W. Experimental Studies of Cascade Phenomena in Metals. In Proceedings of the International Conference on "Evolution of Microstructure in Metals During Irradiation", Chalk River, ON, Canada, 29 September–2 October 1992; Volume 19, pp. 463–466.

120. Vörtler, K.; Juslin, N.; Bonny, G.; Malerba, L.; Nordlund, K. The effect of prolonged irradiation on defect production and ordering in Fe–Cr and Fe–Ni alloys. *J. Phys. Condens. Matter* **2011**, *23*, 355007. [CrossRef] [PubMed]

121. Zinkle, S.; Snead, L. Designing Radiation Resistance in Materials for Fusion Energy. *Annu. Rev. Mater. Res.* **2014**, *44*, 241–267. [CrossRef]

122. Zinkle, S. Radiation-Induced Effects on Microstructure. In *Comprehensive Nuclear Materials*; Elsevier: Amsterdam, The Netherlands, 2012; pp. 65–98.

123. Pickering, E.J.; Carruthers, A.W.; Barron, P.J.; Middleburgh, S.C.; Armstrong, D.E.; Gandy, A.S. High-Entropy Alloys for Advanced Nuclear Applications. *Entropy* **2021**, *23*, 98. [CrossRef] [PubMed]

124. Brown, A.; Ashby, M. Correlations for Diffusion Constants. *Acta Metall.* **1980**, *28*, 1085–1101. [CrossRef]

125. El-Atwani, O.; Li, N.; Li, M.; Devaraj, A.; Baldwin, J.K.S.; Schneider, M.M.; Martinez, E. Outstanding radiation resistance of tungsten-based high-entropy alloys. *Sci. Adv.* **2019**, *5*, eaav2002. [CrossRef] [PubMed]

126. Zhang, Z.; Han, E.-H.; Xiang, C. Irradiation behaviors of two novel single-phase bcc-structure high-entropy alloys for accident-tolerant fuel cladding. *J. Mater. Sci. Technol.* **2021**, *84*, 230–238. [CrossRef]

127. Li, R.; Xie, L.; Wang, W.Y.; Liaw, P.K.; Zhang, Y. High-Throughput Calculations for High-Entropy Alloys: A Brief Review. *Front. Mater.* **2020**, *7*, 290. [CrossRef]

128. Feng, R.; Zhang, C.; Gao, M.C.; Pei, Z.; Zhang, F.; Chen, Y.; Ma, D.; An, K.; Poplawsky, J.D.; Ouyang, L.; et al. High-throughput design of high-performance lightweight high-entropy alloys. *Nat. Commun.* **2021**, *12*, 4329. [CrossRef] [PubMed]

129. Feng, R.; Feng, B.J.; Gao, M.C.G.; Zhang, C.; Neuefeind, J.C.; Poplawsky, J.D.; Ren, Y.; An, K.; Widom, M.; Liaw, P.K. Superior High-Temperature Strength in a Supersaturated Refractory High-Entropy Alloy. *Adv. Mater.* **2021**, *33*, e2102401. [CrossRef]

130. Yan, X.H.; Liaw, P.K.; Zhang, Y. Ultrastrong and ductile BCC high-entropy alloyswith low-density via dislocation regulation andnanoprecipitates. *J. Mater. Sci. Technol.* **2022**, *110*, 109–116. [CrossRef]